Quantum interference in superconducting wire networks and Josephson junction arrays: An analytical approach based on multiple-loop Aharonov-Bohm Feynman path integrals

Yeong-Lieh Lin[1] and Franco Nori[2,3,*]
[1]*Department of Physics, West Virginia University, Morgantown, West Virginia 26506-6315*
[2]*Frontier Research System, The Institute of Physical and Chemical Research (RIKEN), Saitama 351-0198, Japan*
[3]*Center for Theoretical Physics, Physics Department, Center for the Study of Complex Systems, The University of Michigan, Ann Arbor, Michigan 48109-1120*

(Received 30 November 2001; published 20 May 2002)

We investigate analytically and numerically the mean-field superconducting-normal phase boundaries of two-dimensional superconducting wire networks and Josephson junction arrays immersed in a transverse magnetic field. The geometries we consider include square, honeycomb, triangular, and kagomé lattices. Our approach is based on an analytical study of multiple-loop Aharonov-Bohm effects: the quantum interference between different electron closed paths where each one of them encloses a net magnetic flux. Specifically, we compute exactly the sums of magnetic phase factors, i.e., the lattice path integrals, on all closed lattice paths of different lengths. A very large number, e.g., up to 10^{81} for the square lattice, of exact lattice path integrals are obtained. Analytic results of these lattice path integrals then enable us to obtain the resistive transition temperature as a continuous function of the field. In particular, we can analyze measurable effects on the superconducting transition temperature $T_c(B)$ as a function of the magnetic field B, originating from the electron trajectories over loops of various lengths. In addition to systematically deriving previously observed features and understanding the physical origin of the dips in $T_c(B)$ as a result of multiple-loop quantum interference effects, we also find novel results. In particular, we explicitly derive the self-similarity in the phase diagram of square networks. Our approach allows us to analyze the complex structure present in the phase boundaries from the viewpoint of quantum interference effects due to the electron motion on the underlying lattices. The physical origin of the structures in the phase diagrams is derived in terms of the size of regions of the lattice explored by the electrons. Namely, the larger the region of the sample the electrons can explore (and thus the larger the number of paths the electron can take), the finer and sharper structure appears in the phase boundary. Our results for kagomé and honeycomb lattices compare very well with recent experimental measurements by Xiao *et al.* [preceding paper, Phys. Rev. B **65**, 214503 (2001)].

DOI: 10.1103/PhysRevB.65.214504 PACS number(s): 74.50.+r

I. INTRODUCTION

When immersed in an externally applied magnetic field, superconducting networks[1] made of thin wires, proximity-effect junctions, and tunnel junctions exhibit complex and interesting forms of phase diagrams. These superconducting networks have been studied in various kinds of geometries, including simple[1] and complex[2,3] periodic lattices, regular fractals,[4] bond-percolation networks,[5] disordered arrays,[6] and quasiperiodic lattices.[7–11] The rich structure present in the resistive transition temperature as a function of the magnetic field, namely, the superconducting-normal phase diagram, has a rich structure that has been the subject of various experimental and theoretical investigations.[9,12–16]

A. Physics of the phase diagram

The rich structure in the phase diagram is essentially a result of the quantum interference effect or frustration due to the magnetic field and the built-in multiconnectedness of the networks. The magnetic fluxes through the cells of various areas, measured in units of the superconducting flux quantum $\Phi_0 \equiv hc/2e$, are useful parameters to characterize the interference effect. At zero magnetic field, the quantum interference effect is absent, and therefore the resistive transition temperature should have a peak. Also, due to gauge invariance, physical quantities should be periodic functions of the cell fluxes, with a period of Φ_0. These arguments qualitatively explain the apparent periodic or quasiperiodic structures observed in phase diagrams of networks of various geometries.

To gain a quantitative description of the phase diagrams, we employ the mean-field theory which is very effective in serving such a purpose. For wire networks, the mean-field expression is given by the Landau-Ginsburg equation expressed in terms of the order parameters at the nodes.[12] For a junction array, one has a set of self-consistent equations[13,14] for the thermally averaged pair wave functions of the grains. Such equations are linearized near the transition point, and the highest temperature at which a nontrivial solution first appears is identified as the transition temperature. Therefore, one is left to find the top spectral edge of eigenvalue problems. The equations for a junction array can be mapped onto a tight-binding Schrödinger problem for an electron hopping on a lattice immersed in a magnetic field. The equations for a wire network are in general more difficult to solve, because the eigenvalue appears in a nonlinear way.

Numerical results have been obtained for phase diagrams of networks of various geometries. All of them compare very well with the corresponding experimental data; the locations of the peaks of various sizes are correctly predicted and the relative heights of the peaks are also reproduced with occa-

sional small deviations. The success of mean-field theory[14,15] suggests that much of the frustration effect in a statistical problem can be accounted for in terms of quantum interference effect of linear wave mechanics.

B. Many-loop generalization of the standard Aharonov-Bohm effect

In this paper, we systematically investigate the field-dependent superconducting-normal phase for a variety of two-dimensional superconducting networks. The basis of our approach is an analytic study of electron quantum interference effects originating from sums over magnetic phase factors on closed lattice paths. The sums of these phase factors, called lattice path integrals, are many-loop generalizations of the standard one-loop Aharonov-Bohm-type argument, where the electron wave function picks up a phase factor $e^{i\Phi}$ each time it goes around a closed loop enclosing a net flux Φ.

We compute analytically the lattice path integrals up to very long lengths for various types of lattices. These lattice path integrals contain the quantum interference of enormous numbers of closed paths. Through an iterative approach, these results then enable us to obtain the corresponding phase boundaries[14,15] as continuous functions of the strength of the applied field. This method provides a systematic approximation scheme, through finite truncations, for the spectral edges of eigenvalue problems from which our mean-field phase diagrams can be computed. Thus, we can gain considerable theoretical insight into the physical origin of the structure in the phase diagrams. This approach also enables us to analyze the structure of the phase boundaries from the viewpoint of the geometric features of the networks. We apply this approach to study the phase boundaries of square, honeycomb, triangular, and kagomé lattices. Our studies provide a complete and detailed analysis of the relationship between the phase diagram structures and the corresponding network geometries.

C. Organization of the paper

This paper is organized as follows. In Sec. II, we describe the general formulation of our approach to the determination of phase diagrams for a variety of periodic superconducting networks. To illustrate our calculational scheme, we first compute the Little-Parks oscillatory phase boundary of a single superconducting loop in Sec. III. In Sec. IV, we apply this approach to the superconducting square network. We devote Sec. V to a discussion of a very important and interesting feature observed in the phase boundary of the square network, namely, the self-similarity. The superconducting honeycomb, triangular, and kagomé networks are studied based on the same approach, respectively, in Secs. VI, VII, and VIII. In Sec. IX, we discuss some general trends in the application of this approach to these types of networks studied above. Comparisons of the phase boundaries between a single superconducting loop and the corresponding superconducting network are also made. Furthermore, we present a brief discussion on the relationship between our approach and other related methods. In Sec. X, we compare the phase boundaries of honeycomb and kagomé lattices. The last section summarizes our results.

II. GENERAL FORMALISM

The physics of $T_c(B)$, the superconducting-normal phase boundary as a function of the field B, is determined by the electronic kinetic energy because the applied field induces a diamagnetic current in the superconductor.[1] This current (proportional to the velocity) determines the kinetic energy of the system. In other words, the kinetic energy can be written in terms of the temperature as

$$-\frac{\hbar^2}{2m^*}\nabla^2 \sim -\frac{\hbar^2}{2m^*\xi(T)^2} \sim T_c(B)-T_c(0),$$

where, for any superconductor, m^* is twice the electron mass and

$$\xi(T)=\frac{\xi(0)}{\sqrt{1-T_c(B)/T_c(0)}}$$

is the temperature-dependent coherence length. The problem of obtaining $T_c(B)$ is then mapped to that of finding the spectral edges of tight-binding electrons on the corresponding lattice. Thus, assuming a unit hopping integral between adjacent sites, we consider the Hamiltonian

$$H=\sum_{\langle ij\rangle} c_i^\dagger c_j \exp(iA_{ij}), \tag{1}$$

which describes the kinetic energy of electrons hopping on a discrete lattice subject to a perpendicular magnetic field. Here $\langle ij\rangle$ refers to nearest-neighbor sites and the magnetic phase

$$A_{ij}=2\pi\int_j^i \mathbf{A}\cdot d\mathbf{l}$$

is 2π times the line integral of the vector potential, **A**, along the bond from j to i in units of the $\Phi_0=hc/2e$.

A. Sums over closed paths

The lattice path integral μ_l is defined as

$$\mu_l \equiv \sum_{\text{all closed lattice paths } \gamma \text{of length l}} e^{i\Phi_\gamma}. \tag{2}$$

By closed paths of length l we mean the paths starting and ending at the same site after traversing l steps on the lattice and Φ_γ is the sum over phases of the bonds on the path γ. Let $|\Psi_i\rangle$ denote a localized electron state centered at site i. It is not difficult to notice that μ_l corresponds precisely to the quantum mechanical expectation value $\langle\Psi_i|H^l|\Psi_i\rangle$, which summarizes the contribution to the electron kinetic energy of *all* closed paths of l steps. The physical meaning of the lattice path integral

$$\mu_l=\langle\Psi_i|H^l|\Psi_i\rangle$$

thus becomes clear. The Hamiltonian H is applied l times to the initial state $|\Psi_i\rangle$, resulting in the new state

$$|\Psi_f\rangle = H^l|\Psi_i\rangle$$

located at the end of the path traversing l lattice bonds. Because of the presence of a magnetic field, a magnetic phase factor $e^{iA_{ij}}$ is acquired by an electron when hopping from j to the adjacent site i. The lattice path integral μ_l is nonzero only when the path ends at the starting site. In other words, μ_l is the sum of the contributions from all *closed* paths of l steps starting and ending at the same site, each one weighted by its corresponding phase factor $e^{i\Phi_\gamma}$ where

$$\frac{\Phi_\gamma}{2\pi} = \textit{net flux enclosed by the closed path}\,\gamma.$$

B. Quantum interference

It is important to stress that Φ_γ depends crucially on the traveling route of the path.[14,15] For instance, Φ_γ will be positive (negative) by traversing a polygon loop counterclockwise (clockwise). Therefore, *quantum interference* information contained in μ_l arises because the phase factors of different closed paths, including those from all kinds of distinct loops and separate contributions from the same loop, interfere with each other. Sometimes, the phases corresponding to subloops of a main path cancel.

To analytically compute[14,15] the lattice path integrals μ_l is in general a difficult task since μ_l involves an enormous number of different paths (growing rapidly when l increases), each one determined by its corresponding net magnetic phase factor. We have developed systematic and efficient methods to calculate the lattice path integrals for a number of distinct lattices. The techniques involve successively iterating the constructed recursion relations and exploiting the symmetries of the underlying lattices. The technical details of the implementation will be presented elsewhere. Below we will only list the first few calculated lattice path integrals in relevant places. Results for the lattice path integrals of larger l will not be presented due to their lengthy expressions, but will be used in some of our calculations.

In summary, the lattice path integrals summarize the electron quantum interference effects originating from sums over magnetic phase factors on closed lattice paths. The sums of these phase factors, the lattice path integrals, are many-loop generalizations of the standard one-loop Aharonov-Bohm-type argument, where the electron wave function picks up a phase factor $e^{i\Phi}$ each time it goes around a closed loop enclosing a net flux Φ.

C. Computation of the energy eigenvalues from lattice path integrals

We now outline the scheme for obtaining the eigenvalues from the calculated lattice path integrals. Let us apply the Hamiltonian to the starting state

$$|\psi_1\rangle \equiv |\Psi_i\rangle,$$

which is a localized state centered at an arbitrary site i on the lattice, and perform the following expansions:

$$H|\psi_1\rangle = a_1|\psi_1\rangle + b_2|\psi_2\rangle$$

and for $n>1$

$$H|\psi_n\rangle = b_n|\psi_{n-1}\rangle + a_n|\psi_n\rangle + b_{n+1}|\psi_{n+1}\rangle.$$

The Hamiltonian matrix in the basis $|\psi_n\rangle$ is obviously in a real tridiagonal form. Each new state in this method expands outward by one more step from the site where the starting state is located. Note that the a_n's and b_{n+1}'s are gauge-invariant quantities. Through these parameters we can construct the truncated Hamiltonian matrices $H^{(n)}$, which are the nth-order approximation to H. For instance,

$$H^{(2)} = \begin{bmatrix} a_1 & b_2 \\ b_2 & a_2 \end{bmatrix},$$

$$H^{(3)} = \begin{bmatrix} a_1 & b_2 & 0 \\ b_2 & a_2 & b_3 \\ 0 & b_3 & a_3 \end{bmatrix},$$

$$H^{(4)} = \begin{bmatrix} a_1 & b_2 & 0 & 0 \\ b_2 & a_2 & b_3 & 0 \\ 0 & b_3 & a_3 & b_4 \\ 0 & 0 & b_4 & a_4 \end{bmatrix},$$

and so on. The quantity we desire, i.e., the top spectral edge, can then be obtained by solving the eigenvalues of $H^{(n)}$ and will be designated by $T_c^{(n)}$, which is the nth-order approximant to the phase boundary. This scheme is useful because finite truncations give good approximations to $T_c(B)$.

The coefficients a_n's and b_{n+1}'s can be exactly expressed in terms of the lattice path integrals in a systematic manner, which will be presented below, respectively, for the bipartite and nonbipartite lattices. In general, given the lattice path integrals up to the order μ_{2L-1}, which contains information on the quantum interference effects due to closed paths of $2L-1$ steps, we can obtain the coefficients up to a_L and b_L. Thus, the Lth-order truncation of the Hamiltonian matrix can be constructed, and subsequently $T_c^{(L)}$ can be obtained.

1. For bipartite lattices

We first discuss the case for bipartite lattices where the lattice path integrals of odd number steps are identically zero, i.e.,

$$\mu_{2l+1} = 0.$$

It is evident that

$$a_n = 0$$

for any n. To compute the b_{n+1}'s, we define an auxiliary matrix B with the first row elements given by

$$B_{1,l} \equiv \mu_{2l}.$$

The other rows are evaluated by using only one immediate predecessor row. Namely, for $k \geqslant 2$ and $l \geqslant 1$

$$B_{k,l} = \frac{B_{k-1,l+1}}{B_{k-1,1}} - \sum_{i=0}^{l-1} B_{k,i} B_{k-1,l-i}, \tag{3}$$

where

$$B_{n,0} \equiv 1$$

for $n \geqslant 1$. The b_{n+1}'s are obtained from the elements of first columns of the matrix B as

$$b_{n+1} = \sqrt{B_{n,1}}. \tag{4}$$

Below we explicitly express the first few b_{n+1}'s in terms of the lattice path integrals noting that μ_2 is always equal to z, the coordination number of the lattice:

$$b_2 = \sqrt{\mu_2} = \sqrt{z},$$

$$b_3 = \sqrt{\frac{\mu_4}{z} - z},$$

$$b_4 = \sqrt{\frac{\mu_6 - 2\mu_4 z + z^3}{\mu_4 - z^2} - \frac{\mu_4 - z^2}{z}}.$$

These expressions are applicable to any type of bipartite lattice.

It is worthwhile to point out that the number of elements on a specific row is always less than that on the immediate predecessor row by 1. For instance, for a specific k, if the matrix elements run from $B_{k,1}$ to $B_{k,l}$, the elements in the next row run from $B_{k+1,1}$ to $B_{k+1,l-1}$. Therefore, given the lattice path integrals up to μ_{2L}, the matrix B consists of L rows. The Lth (last) row has only one element $B_{L,1}$ from which we can deduce b_{L+1}. It is clear now that the highest-order approximation $T_c^{(L+1)}$ to the phase boundary can be obtained from $\mu_2, \mu_4, \ldots, \mu_{2L}$.

2. For nonbipartite lattices

Turning to the nonbipartite lattice case, we now define an auxiliary matrix N with the first row elements given by

$$N_{1,l} \equiv \mu_l.$$

The other rows are evaluated by using only one immediate predecessor row. Namely, for $k \geqslant 2$ and $l \geqslant 1$,

$$N_{k,l} = \frac{N_{k-1,l+2} - N_{k-1,1} N_{k-1,l+1}}{N_{k-1,2} - N_{k-1,1}^2} - \sum_{i=0}^{l-1} N_{k,i} N_{k-1,l-i}, \tag{5}$$

where $N_{n,0} \equiv 1$ for $n \geqslant 1$. The a_n's and b_{n+1}'s are obtained from the elements of the first and second columns as

$$a_n = N_{n,1} \tag{6}$$

and

$$b_{n+1} = \sqrt{N_{n,2} - N_{n,1}^2}. \tag{7}$$

Below we explicitly express the first few a_n's and b_{n+1}'s in terms of the lattice path integrals:

$$a_1 = 0,$$

$$a_2 = \frac{\mu_3}{z},$$

$$a_3 = \frac{\mu_5 z^2 - 2\mu_4 \mu_3 z + \mu_3^3}{\mu_4 z^2 - \mu_3^2 z - z^4}$$

and

$$b_2 = \sqrt{z},$$

$$b_3 = \sqrt{\frac{\mu_4}{z} - \frac{\mu_3^2}{z^2} - z}.$$

The above expressions are valid for any type of nonbipartite lattice.

It is worth stressing that the number of elements on a specific row is always less than that on the immediate predecessor row by 2. For instance, for a specific k, if the matrix elements run from $N_{k,1}$ to $N_{k,l}$, the elements in the next row run from $N_{k+1,1}$ to $N_{k+1,l-2}$. Therefore, given the lattice path integrals up to μ_{2L+1}, the matrix N consists of $L+1$ rows. The Lth row has only three elements $N_{L,1}$, $N_{L,2}$, and $N_{L,3}$, where b_{L+1} can be obtained from $N_{L,2}$, and $N_{L,3}$. The $(L+1)$th (last) row has only one element $N_{L+1,1}$ from which we can deduce a_{L+1}. It is clear now that the highest-order approximation $T_c^{(L+1)}$ to the phase boundary can be obtained from $\mu_1, \mu_2, \ldots, \mu_{2L+1}$.

III. SIMPLE ILLUSTRATION: A SINGLE SUPERCONDUCTING LOOP

Before we study the lattice cases, we apply the formalism described above to three simple single-cell cases. Namely, we calculate, respectively, the transition temperature of a single superconducting loop in the shape of a square, a hexagon, and a triangle. Exact solutions of the phase boundaries can be obtained for these simple cases. For all of these, $\Phi = \phi/2\pi$ stands for the magnetic flux through these elementary cells, in units of Φ_0.

The lattice path integrals μ_l now correspond to the sums over all closed paths of l steps on a single cell. Closed-form results for the lattice path integrals are derived. They are, respectively,

$$\mu_{2l}^{(s)} = C_l^{2l} + 2 \sum_{k=1}^{[l/2]} C_{l-2k}^{2l} \cos(k\phi)$$

on a square,

$$\mu_{2l}^{(h)} = C_l^{2l} + 2 \sum_{k=1}^{[l/3]} C_{l-3k}^{2l} \cos(k\phi)$$

on a hexagon, and

$$\mu_{2l}^{(t)} = C_l^{2l} + 2\sum_{k=1}^{[l/3]} C_{l-3k}^{2l}\cos(2k\phi),$$

$$\mu_{2l+1}^{(t)} = 2\sum_{k=0}^{[(l-1)/3]} C_{l-3k-1}^{2l+1}\cos[(2k+1)\phi]$$

on a triangle. Here

$$C_n^m = \frac{m!}{n!(m-n)!}$$

is the binomial coefficient, and the notation $[x]$ means the largest integer equal to or smaller than x. Through these results for the lattice path integrals, it is straightforward to compute the parameters a_n's and b_{n+1}'s. In fact, for these small simple systems, the iterative process terminates very quickly. In other words, the parameters a_n's and b_{n+1}'s become identically zero after a few iterations. Hence, the corresponding exact tridiagonal Hamiltonian matrices can be readily constructed.

A. Square loop

Denoting the tridiagonal Hamiltonian matrix for the square loop by H_s, we find that

$$H_s = \sqrt{2}\begin{bmatrix} 0 & 1 & 0 & 0 \\ 1 & 0 & \left|\cos\left(\frac{\phi}{2}\right)\right| & 0 \\ 0 & \left|\cos\left(\frac{\phi}{2}\right)\right| & 0 & \left|\sin\left(\frac{\phi}{2}\right)\right| \\ 0 & 0 & \left|\sin\left(\frac{\phi}{2}\right)\right| & 0 \end{bmatrix},$$

which is obtained by using only μ_2, μ_4, and μ_6. A closed-form expression for the top eigenvalue of H_s can be easily obtained:

$$T_c(\phi) = \sqrt{2+2\cos\left(\frac{\phi}{2}\right)}.$$

B. Hexagonal loop

Similarly, denoting the tridiagonal Hamiltonian matrix for the hexagon loop by H_h, we find that

$$H_h = \begin{bmatrix} 0 & \sqrt{2} & 0 & 0 & 0 & 0 \\ \sqrt{2} & 0 & 1 & 0 & 0 & 0 \\ 0 & 1 & 0 & \sqrt{1+\cos(\phi)} & 0 & 0 \\ 0 & 0 & \sqrt{1+\cos(\phi)} & 0 & \sqrt{1-\cos(\phi)} & 0 \\ 0 & 0 & 0 & \sqrt{1-\cos(\phi)} & 0 & 1 \\ 0 & 0 & 0 & 0 & 1 & 0 \end{bmatrix},$$

which is obtained by using only μ_2, μ_4, μ_6, μ_8, and μ_{10}. Let j be an integer; the top eigenvalue of H_h can be expressed as follows:

$$T_c(\phi) = \begin{cases} \sqrt{2+2\cos\left(\frac{\phi}{3}+\frac{2\pi}{3}\right)} & \text{for } -\frac{3}{2}+3j \leqslant \frac{\phi}{2\pi} \leqslant -\frac{1}{2}+3j, \\ 2\cos\left(\frac{\phi}{6}\right) & \text{for } -\frac{1}{2}+6j \leqslant \frac{\phi}{2\pi} \leqslant \frac{1}{2}+6j, \\ \sqrt{2+2\cos\left(\frac{\phi}{3}-\frac{2\pi}{3}\right)} & \text{for } \frac{1}{2}+3j \leqslant \frac{\phi}{2\pi} \leqslant \frac{3}{2}+3j, \\ -2\cos\left(\frac{\phi}{6}\right) & \text{for } \frac{5}{2}+6j \leqslant \frac{\phi}{2\pi} \leqslant \frac{7}{2}+6j. \end{cases}$$

C. Triangular loop

Denoting the tridiagonal Hamiltonian matrix for the triangle loop by H_t, we find that

$$H_t = \begin{bmatrix} 0 & \sqrt{2} & 0 \\ \sqrt{2} & \cos(\phi) & |\sin(\phi)| \\ 0 & |\sin(\phi)| & -\cos(\phi) \end{bmatrix},$$

which is obtained by using only $\mu_1-\mu_5$. The top eigenvalue of H_t can be expressed as follows:

$$T_c(\phi)=\begin{cases} 2\cos\left(\dfrac{\phi}{3}+\dfrac{2\pi}{3}\right) & \text{for } -\dfrac{3}{2}+3j\leqslant\dfrac{\phi}{2\pi}\leqslant-\dfrac{1}{2}+3j, \\ 2\cos\left(\dfrac{\phi}{3}\right) & \text{for } -\dfrac{1}{2}+3j\leqslant\dfrac{\phi}{2\pi}\leqslant\dfrac{1}{2}+3j, \\ 2\cos\left(\dfrac{\phi}{3}-\dfrac{2\pi}{3}\right) & \text{for } \dfrac{1}{2}+3j\leqslant\dfrac{\phi}{2\pi}\leqslant\dfrac{3}{2}+3j. \end{cases}$$

In Fig. 1, we plot the superconducting transition temperature, $\Delta T_c(\Phi)\equiv T_c(0)-T_c(\Phi)=2-T_c(\Phi)$, respectively, of a square loop, a hexagon loop, and a triangle loop for $-2\leqslant\Phi\leqslant2$. It is evident that these phase diagrams are qualitatively identical. Also, the $\Delta T_c(\Phi)$ shown are periodic functions of Φ and the period of the oscillation in the flux is equal to Φ_0. As expected, $\Delta T_c(\Phi)$ have their minima at $\Phi=j\Phi_0$ and their maxima at $\Phi=j\Phi_0/2$.

It is interesting to note that $\Delta T_c(\Phi)$ has the largest magnitude for the triangular loop and the smallest for the hexagonal loop. It will be seen in Sec. X that this one-loop general behavior carries over to the network cases, in spite of the distinctive differences in the fine structure of their phase boundaries. These results are consistent with the ones obtained numerically in Ref. 2.

IV. SQUARE LATTICE

For the square lattice, we denote the lattice path integrals by s_{2l}. In other words, s_{2l} is the exact sum of the phase factors of all $2l$-step closed paths on the square lattice. Below $\phi/2\pi$ corresponds to the magnetic flux through an elementary square plaquette, i.e.,

$$\frac{\phi}{2\pi}=c^2B.$$

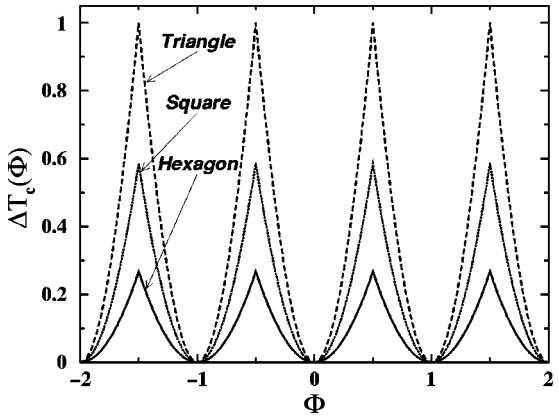

FIG. 1. The oscillatory phase boundary $\Delta T_c(\Phi)$ for a single superconducting loop. The top curve corresponds to a triangle (dashed line) the middle a square (dotted line), and the bottom a hexagon (solid line). Φ is the magnetic flux through these cells in units of Φ_0.

Throughout this paper, c denotes the lattice constant of all the lattices considered in this work. The results for $s_2, s_4, \ldots, s_{12}$ are

$$s_2=4,$$

$$s_4=28+8\cos\phi,$$

$$s_6=232+144\cos\phi+24\cos2\phi,$$

$$s_8=2156+2016\cos\phi+616\cos2\phi+96\cos3\phi+16\cos4\phi,$$

$$s_{10}=21944+26320\cos\phi+11080\cos2\phi+3120\cos3\phi+840\cos4\phi+160\cos5\phi+40\cos6\phi,$$

$$s_{12}=240280+337560\cos\phi+174384\cos2\phi+67256\cos3\phi+23928\cos4\phi+7272\cos5\phi+2400\cos6\phi+528\cos7\phi+144\cos8\phi+24\cos9\phi.$$

We have computed the lattice path integrals for the square lattice up to s_{138}, which are obtained by *exactly summing up* $\sim10^{81}$ closed paths. The first few lattice path integrals can be quickly obtained analytically by hand. We have used MAPLE symbolic manipulation software to obtain lattice path integrals of longer lengths. For these, it is convenient to optimize the algorithm by exploiting the symmetries of the problem. These calculated lattice path integrals s_{2l}'s have enabled us to obtain the phase boundary up to $T_c^{(70)}(\phi)$.

It is instructive to explain how the first few lattice path integrals are obtained. This will also clarify their physical meaning. Since there is no path of one step for returning an electron to its initial site, s_1 is always equal to zero. Indeed, all lattice path integrals s_{2l+1} involving an odd number of steps are equal to zero. Now let us compute the next lattice path integral, with two steps. There are four closed paths of two steps each [retracing each other on one bond $(\cdot\leftrightarrow)$, where the dot $\cdot$ indicates the initial site], thus

$$s_2=4\cdot\leftrightarrow=4e^{i0\phi}=4=z,$$

where z is the coordination number of the lattice.

There are 28 closed paths of four steps each: four retracing twice on one bond $(\overset{\leftrightarrow}{\cdot\leftrightarrow})$, 12 starting from a site connecting two adjacent bonds and retracing once on each bond $(\leftrightarrow\cdot\leftrightarrow)$, and 12 moving two bonds away and then two

bonds back to the original site ($\overleftarrow{\cdot}\overleftarrow{\cdot}\overrightarrow{\cdot}\overrightarrow{\cdot}$). Since all of them enclose no area (i.e., no flux), then

$$s_4^{\text{no flux}} = 4\,\overleftrightarrow{\cdot}\overleftrightarrow{\cdot} + 12 \leftrightarrow \cdot \leftrightarrow + 12\,\overleftarrow{\cdot}\overleftarrow{\cdot}\overrightarrow{\cdot}\overrightarrow{\cdot} = 28.$$

Among the four-step closed paths, eight of them enclose adjacent square cells (four counterclockwise and four clockwise) contributing

$$4e^{i\phi} + 4e^{-i\phi} = 8\cos\phi$$

to s_4. Thus it follows that $s_4 = 28 + 8\cos\phi$. Higher-order integrals s_{2l} can be similarly constructed.

It is straightforward to compute the nonzero parameters b_n from the obtained results for s_{2l}. The corresponding truncated Hamiltonians $H^{(n)}$ can then be readily constructed. For instance, the second-order truncation of the Hamiltonian is

$$H^{(2)} = \begin{bmatrix} 0 & 2 \\ 2 & 0 \end{bmatrix}.$$

Its corresponding top eigenvalue is $T_c^{(2)}(\phi) = 2$, which does not depend on ϕ. This is understandable from the fact that the shortest length for a closed path on the square lattice to enclose the magnetic flux is for $l = 4$ while $H^{(2)}$ only contains elements derived from μ_2. The third-order truncation of the Hamiltonian is

$$H^{(3)} = \begin{bmatrix} 0 & 2 & 0 \\ 2 & 0 & \sqrt{3 + 2\cos\phi} \\ 0 & \sqrt{3 + 2\cos\phi} & 0 \end{bmatrix}.$$

Its corresponding top eigenvalue is

$$T_c^{(3)}(\phi) = \sqrt{7 + 2\cos\phi}.$$

The fourth-order truncation of the Hamiltonian, $H^{(4)}$, is

$$\begin{bmatrix} 0 & 2 & 0 & 0 \\ 2 & 0 & \sqrt{3 + 2\cos\phi} & 0 \\ 0 & \sqrt{3 + 2\cos\phi} & 0 & \sqrt{\dfrac{3 + 8\cos\phi + 8\cos^2\phi}{3 + 2\cos\phi}} \\ 0 & 0 & \sqrt{\dfrac{3 + 8\cos\phi + 8\cos^2\phi}{3 + 2\cos\phi}} & 0 \end{bmatrix}.$$

Its corresponding top eigenvalue is

$$T_c^{(4)}(\phi) = \sqrt{2}\sqrt{\frac{3\cos^2\phi + 7\cos\phi + 6 + \alpha}{3 + 2\cos\phi}},$$

where

$$\alpha = \sqrt{9\cos^4\phi + 26\cos^3\phi + 45\cos^2\phi + 54\cos\phi + 27}.$$

In Fig. 2, we show the superconducting transition temperatures

$$\Delta T_c^{(n)}(\Phi) = T_c(0) - T_c^{(n)}(\Phi)$$

as functions of $\Phi \equiv \phi/2\pi$ for various values of n for the square network obtained from the truncated Hamiltonians $H^{(n)}$. Here $T_c(0)$ equals 4, which is the largest eigenvalue of tight-binding electrons confined on the square lattice in the absence of a magnetic field. It is important to stress that as the order of approximation is increased, more geometrical information of the lattice is included in the interference treatment and more fine structures are resolved. At every step, i.e., for a given size of the network, we can observe the corresponding dips appearing and then becoming sharper. We emphasize that our highest-order approximant $T_c^{(70)}(\Phi)$ has closely reached the infinite-system-size limit $\Delta T_c(\Phi)$. The flux values where the cusps and dips occur have also been labeled.

V. SELF-SIMILARITY IN THE PHASE BOUNDARY OF THE SUPERCONDUCTING SQUARE WIRE NETWORK

In this section, we explicitly demonstrate an important property: the self-similarity of the phase boundary of the superconducting square wire network. This is exemplified in Fig. 3, where we use $\Delta T_c^{(70)}(\Phi)$ for $\Delta T_c(\Phi)$ and omit the superscript. In (a), we plot $\Delta T_c(\Phi)$ for Φ in the interval between 0 and 1. In (b) and (c), we plot $\Delta T_c(\Phi)$ for Φ, respectively, in the ranges $[0.333 \simeq 1/3, 0.4765]$ and $[0.5235, 0.667 \simeq 2/3]$. Figures 3(b) and 3(c) can be regarded as the first generation of the original diagram (a), in the sense that (b) is enlarged from the maximum in the left part of (a) and (c) is enlarged from the maximum in the right part of (a).

This enlargement process is continued as follows: (d) with $\Phi \in [0.375 = 3/8, 0.3978]$ and (e) with $\Phi \in [0.4025, 0.4286 \simeq 3/7]$ are, respectively, the enlargements of the left and right maxima of (b). Similarly, (f) with $\Phi \in [0.5714 \simeq 4/7, 0.5975]$ and (g) with $\Phi \in [0.6022, 0.625 = 5/8]$ are, respectively, the enlargements of the left and right maxima of

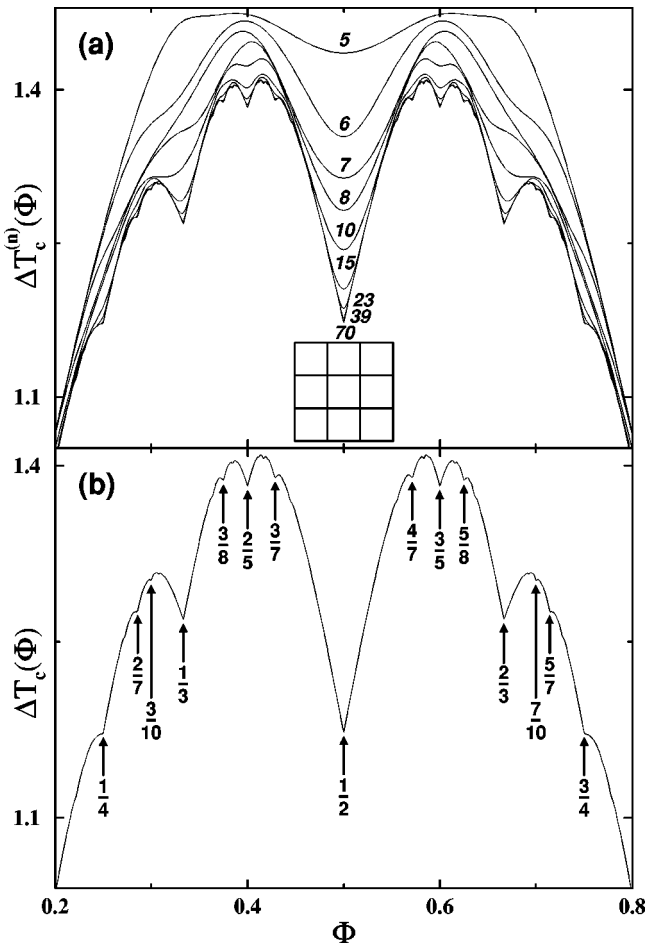

FIG. 2. Superconducting transition temperature for the square network as a continuous function of the applied magnetic field: $\Delta T_c^{(n)}(\Phi)=T_c(0)-T_c^{(n)}(\Phi)$ vs Φ, the magnetic flux through an elementary square cell. In (a) we show the superconducting-normal phase boundaries computed from the truncated Hamiltonians $H^{(n)}$ for Φ in the range between 0.2 and 0.8. We omit the parts of $\Delta T_c^{(n)}(\Phi)$ for $\Phi\in[0,0.2]$ and $[0.8,1]$ since there are no interesting features in these portions of $\Delta T_c^{(n)}(\Phi)$. From top to bottom, the orders of truncation are $n=5$ (top curve), 6, 7, 8, 10, 15, 23, 39, and 70. Note the development of fine structures and cusps. The convergence is monotonic. Note also that the closeness between the curves for $\Delta T_c^{(39)}(\Phi)$ and $\Delta T_c^{(70)}(\Phi)$ implies that $\Delta T_c^{(70)}(\Phi)$ has achieved close convergence to the infinite system size $\Delta T_c(\Phi)$. The inset schematically depicts a square lattice. In (b), we plot $\Delta T_c(\Phi)$ for $\Phi\in[0.2,0.8]$ and label the values of the magnetic flux where observable cusps and dips occur. They include $\Phi=1/4$, 2/7, 3/10, 1/3, 3/8, 2/5, 3/7, 1/2, 4/7, 3/5, 5/8, 2/3, 7/10, 5/7, and 3/4. Here $\Delta T_c(\Phi)\equiv\Delta T_c^{(70)}(\Phi)=T_c(0)-T_c^{(70)}(\Phi)$, our calculated highest-order approximant.

(c). Figures 3(d), 3(e), 3(f), and 3(g) can be regarded as the second generation of the original phase diagram (a). In this way, it is straightforward to deduce that the third generation of (a) will consist of eight phase diagrams: each of (d), (e), (f), and (g) contributes two diagrams. It is evident that these phase diagrams resemble one another except that the phase diagrams gradually become asymmetric.

As shown in these figures, we also label the values of Φ indicating the cusps and dips in $\Delta T_c(\Phi)$. These nine flux values are characteristic of each phase diagram. Indeed, there are general relations between these sets of flux values in different generations. Let $\{p_0/q_0\}$ represent the set of these flux values in (a), i.e., $p_0/q_0=1/4$, 2/7, 1/3, 2/5, 1/2, 3/5, 2/3, 5/7, and 3/4. Denoting the set of characteristic flux values in any of the phase diagrams in the first generation by $\{p_1/q_1\}$, we find that the corresponding flux values in (b) are given by

$$\frac{p_1}{q_1}=\frac{q_0}{3q_0-p_0},$$

and those in (c) are given by

$$\frac{p_1}{q_1}=\frac{p_0+q_0}{p_0+2q_0}.$$

For instance, given $p_0/q_0=1/2$ in (a), we have the corresponding

$$p_1/q_1=2/(6-1)=2/5$$

in (b) and

$$p_1/q_1=(1+2)/(1+4)=3/5$$

in (c). Furthermore, let $\{p_2/q_2\}$ stand for the sets of the corresponding flux values in the second-generation diagrams. In the second-generation diagrams [(d)–(g)] only five characteristic cusps and dips out of nine are observable. There we find that the p_2/q_2 in (d) are related to the p_1/q_1 in (b) by

$$\frac{p_2}{q_2}=\frac{q_1}{3q_1-p_1},$$

p_2/q_2 in (e) are related to p_1/q_1 in (c) by $p_2/q_2=q_1/(3q_1-p_1)$, p_2/q_2 in (f) are related to p_1/q_1 in (b) by

$$\frac{p_2}{q_2}=\frac{p_1+q_1}{p_1+2q_1},$$

and p_2/q_2 in (g) are related to p_1/q_1 in (c) by $p_2/q_2=(p_1+q_1)/(p_1+2q_1)$.

We now summarize our construction of the hierarchy of these phase diagrams. As discussed previously, every diagram can generate two diagrams to the next generation: one is enlarged from the left maximum and the other from the right maximum of this diagram. Thus, starting from the original phase diagram, i.e., $\Delta T_c(\Phi)$ for $\Phi\in[0,1]$, we can generate 2^n diagrams to the nth generation for $n\geqslant 1$. Furthermore, each diagram covers a distinct range of Φ from $\Phi_{\min}$ to $\Phi_{\max}$. Let us arrange these diagrams in the following way, as we did in Fig. 3. We put all the diagrams belonging to the same generation in a row in such an order that from the left to the right $\Phi_{\min}$ (or $\Phi_{\max}$) increases from the smallest to the largest. It is evident that half of them (2^{n-1} diagrams) have $\Phi_{\max}<1/2$ and the other half have $\Phi_{\min}>1/2$. It is not difficult to see that this kind of arrangement will be automatically satisfied in the following way. Following the same order of the diagrams in the previous generation and using them one by one, we put two new generated diagrams

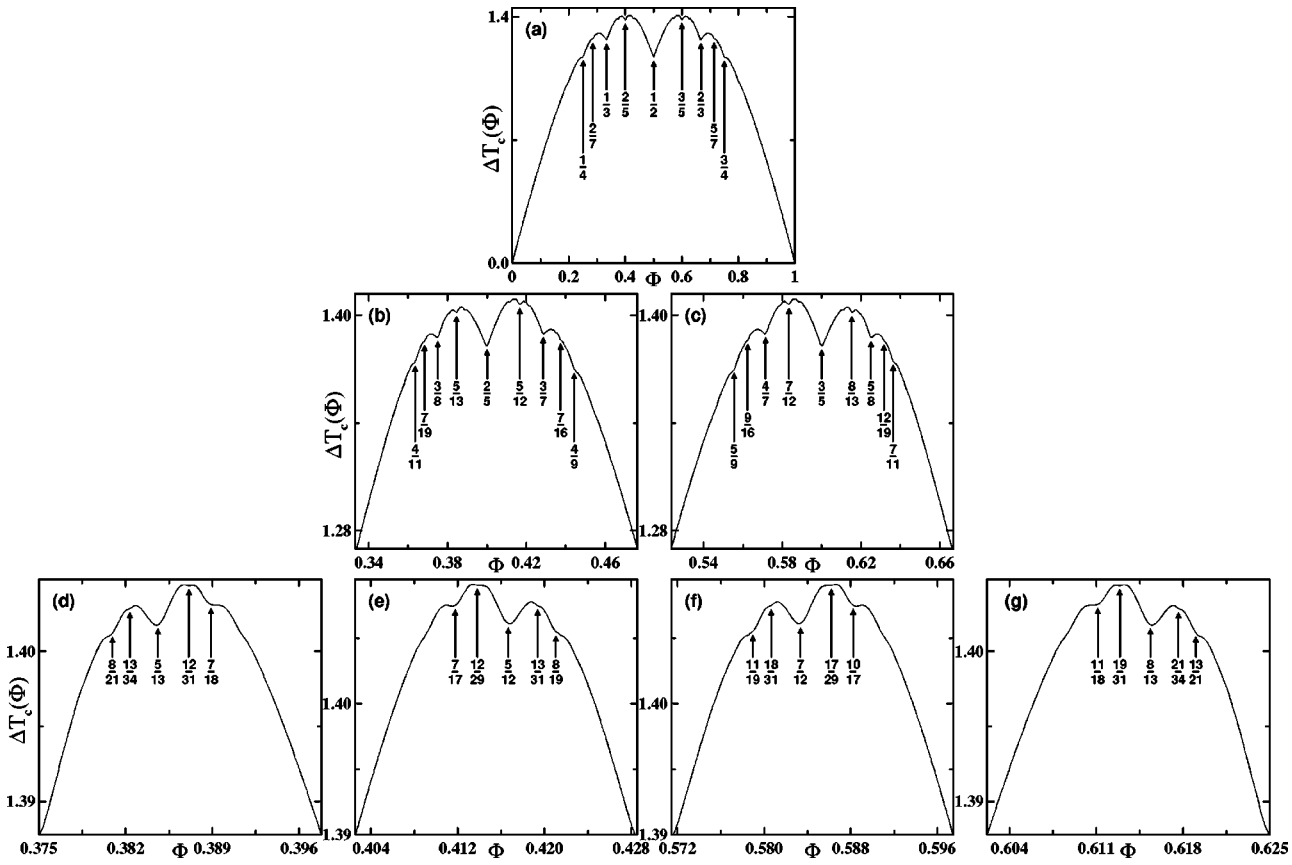

FIG. 3. Field-dependent transition temperature $\Delta T_c(\Phi)$ of the superconducting square network for various different ranges of Φ from (a) to (g), respectively, $\Phi \in [0,1]$, $[0.333 \simeq 1/3, 0.4765]$, $[0.5235, 0.667 \simeq 2/3]$, $[0.375 = 3/8, 0.3978]$, $[0.4025, 0.4286 \simeq 3/7]$, $[0.5714 \simeq 4/7, 0.5975]$, and $[0.6022, 0.625 = 5/8]$. It is clear that (b) is enlarged from the maximum in the left part of (a) and (c) is enlarged from the maximum in the right part of (a). Similarly, (d) and (e) are, respectively, the enlargements of the left and right maxima of (b) while (f) and (g) are, respectively, the enlargements of the left and right maxima of (c). We also include the labeling of the values of Φ where there are cusps and dips in $\Delta T_c(\Phi)$. For the relations between these sets of flux values in different frames, see the text. The self-similarity in the phase boundary can be concluded from the resemblance of these figures though an asymetry in the height develops in each successive magnification.

side by side with the one from the left maximum to the left and the one from the right maximum to the right. It is interesting to notice that, for each generation, the diagrams located at the left part of $\Phi = 1/2$ are mirror images of those located at the right part. This symmetry originates from the property that the phase diagram of $\Delta T_c(\Phi)$ with $\Phi \in [0,1]$ is symmetric around $\Phi = 1/2$.

Indeed, there are one-to-one correspondences between the sets of the characteristic flux values, where cusps and dips in the phase boundaries occur, in different generations. Let us label the diagrams from left to right in the nth generation by $\mathcal{D}_i^{(n)}$ with i running from 1 to 2^n. Similarly, the diagrams in the $(n+1)$th generation are labeled by $\mathcal{D}_i^{(n+1)}$ with i running from 1 to 2^{n+1}. Now let $\{p_n/q_n\}$ represent the sets of the flux values characterizing the cusps and dips in $\Delta T_c(\Phi)$ in any of the phase diagrams in the nth generation and $\{p_{n+1}/q_{n+1}\}$ be the sets belonging to the diagrams in the $(n+1)$th generation. The relations between the (p_{n+1}/q_{n+1})'s and the (p_n/q_n)'s are as follows. For $1 \leqslant i \leqslant 2^n$, the p_{n+1}/q_{n+1} in the diagram $\mathcal{D}_i^{(n+1)}$ [one of the diagrams in the $(n+1)$th generation that located on the left-hand side of $\Phi = 1/2$] is related to the p_n/q_n in $\mathcal{D}_i^{(n)}$ by

$$\frac{p_{n+1}}{q_{n+1}} = \frac{q_n}{3q_n - p_n},$$

and for $2^n + 1 \leqslant i \leqslant 2^{n+1}$, the p_{n+1}/q_{n+1} in the diagram $\mathcal{D}_i^{(n+1)}$ [the second half of the diagrams in the $(n+1)$th generation that located on the right-hand side of $\Phi = 1/2$] is related to the p_n/q_n in $\mathcal{D}_{i-2^n}^{(n)}$ by

$$\frac{p_{n+1}}{q_{n+1}} = \frac{p_n + q_n}{p_n + 2q_n}.$$

Self-similarity in the $\Delta T_c(\Phi)$ curve is a consequence of the fractal energy spectrum of Bloch electrons in a magnetic field which was examined in detail by Hofstadter.[17] However, as far as we are aware, the explicit derivation of the self-similarity of the measurable part, the lowest-energy state, was not presented before.

Recently, the influence of classical chaos on this so-called "Hofstadter's butterfly" has been studied.[18] Furthermore, a semiclassical theory for the dynamics of electrons in a magnetic Bloch band has been developed and used to explain the clustering structure of the spectrum.[19]

VI. HONEYCOMB LATTICE

For the honeycomb lattice, we denote the lattice path integrals by h_{2l}. In other words, h_{2l} is the exact sum of the phase factors of all $2l$-step closed paths on the honeycomb lattice. In this section, $\phi/2\pi$ corresponds to the magnetic flux through an elementary honeycomb plaquette, i.e.,

$$\frac{\phi}{2\pi}=\frac{3\sqrt{3}c^2B}{2\Phi_0}.$$

The results for $h_2, h_4, \ldots, h_{20}$ are

$$h_2=3,$$

$$h_4=15,$$

$$h_6=87+6\cos\phi,$$

$$h_8=543+96\cos\phi,$$

$$h_{10}=3543+1080\cos\phi+30\cos 2\phi,$$

$$h_{12}=23859+10560\cos\phi+726\cos 2\phi+24\cos 3\phi,$$

$$h_{14}=164769+96096\cos\phi+11130\cos 2\phi+798\cos 3\phi+42\cos 4\phi,$$

$$h_{16}=1162719+839040\cos\phi+138720\cos 2\phi+15648\cos 3\phi+1536\cos 4\phi+96\cos 5\phi,$$

$$h_{18}=8363895+7143210\cos\phi+1537668\cos 2\phi+237714\cos 3\phi+33246\cos 4\phi+3834\cos 5\phi+252\cos 6\phi+18\cos 7\phi,$$

$$h_{20}=61216275+59862000\cos\phi+15829200\cos 2\phi+3103320\cos 3\phi+555390\cos 4\phi+89520\cos 5\phi+10920\cos 6\phi+1320\cos 7\phi+120\cos 8\phi.$$

Notice that h_2 and h_4 involve paths that enclose zero net flux. There are three closed paths of two-steps each. Thus, $h_2=3$, the coordination number of the lattice. h_6 is the first lattice path integral with a net flux (in this case flux through one hexagon). There are three counterclockwise and three clockwise six-step paths going through a hexagon. Thus, the term $6\cos\phi$ in h_6. It is possible to derive the first few path integrals analytically ''by hand'' by just counting paths and keeping track of the enclosed flux. The longer-length ones can be computed via symbolic manipulation software.

We have computed the lattice path integrals for the honeycomb lattice up to h_{206}, which are obtained by *exactly* summing up $\sim 10^{96}$ closed paths. These calculated h_{2l}'s have enabled us to obtain the phase boundary up to $T_c^{(104)}(\phi)$.

It is straightforward to compute the nonzero parameters b_n from the obtained results for h_{2l}. The corresponding truncated Hamiltonians $H^{(n)}$ can then be readily constructed. For instance, the second-order truncation of the Hamiltonian is

$$H^{(2)}=\begin{bmatrix}0 & \sqrt{3}\\ \sqrt{3} & 0\end{bmatrix}.$$

Its corresponding top eigenvalue is $T_c^{(2)}=\sqrt{3}$. The third-order truncation of the Hamiltonian is

$$H^{(3)}=\begin{bmatrix}0 & \sqrt{3} & 0\\ \sqrt{3} & 0 & \sqrt{2}\\ 0 & \sqrt{2} & 0\end{bmatrix}.$$

Its corresponding top eigenvalue is $T_c^{(3)}=\sqrt{5}$. Both $T_c^{(2)}$ and $T_c^{(3)}$ are independent of ϕ. This is understandable from the fact that the shortest length for a closed path on the honeycomb lattice to enclose the magnetic flux is for $l=6$ while $H^{(2)}$ and $H^{(3)}$ only contain elements derived from μ_2 and μ_4. The fourth-order truncation of the Hamiltonian is

$$H^{(4)}=\begin{bmatrix}0 & \sqrt{3} & 0 & 0\\ \sqrt{3} & 0 & \sqrt{2} & 0\\ 0 & \sqrt{2} & 0 & \sqrt{2+\cos\phi}\\ 0 & 0 & \sqrt{2+\cos\phi} & 0\end{bmatrix}.$$

Its corresponding top eigenvalue is

$$T_c^{(4)}(\phi)=\frac{1}{2}\sqrt{14+2\cos\phi+2\sqrt{25+2\cos\phi+\cos^2\phi}}.$$

In Fig. 4, we show the superconducting transition temperatures $\Delta T_c^{(n)}(\Phi)=T_c(0)-T_c^{(n)}(\Phi)$ as functions of $\Phi\equiv\phi/2\pi$ for various n for the honeycomb network obtained from the truncated Hamiltonians $H^{(n)}$. Here $T_c(0)$ equals 3, which is the largest eigenvalue of tight-binding electrons confined on the honeycomb lattice in the absence of a magnetic field.

We observe that as the order of approximation is increased, more geometrical information of the lattice is included in the *interference treatment* and more fine structures are resolved. This explains *the origin of the fine structure observed*: the more geometric information on the lattice is explored by the paths of the electrons, the sharper the fine structures.

We emphasize that our highest-order approximant $T_c^{(104)}(\Phi)$ has closely reached the infinite-system-size limit $\Delta T_c(\Phi)$. The flux values where the cusps and dips occurred have also been labeled. In general, besides the cusp at $\Phi=1/2$, there are cusps at

$$\Phi=\frac{m}{2m+1}$$

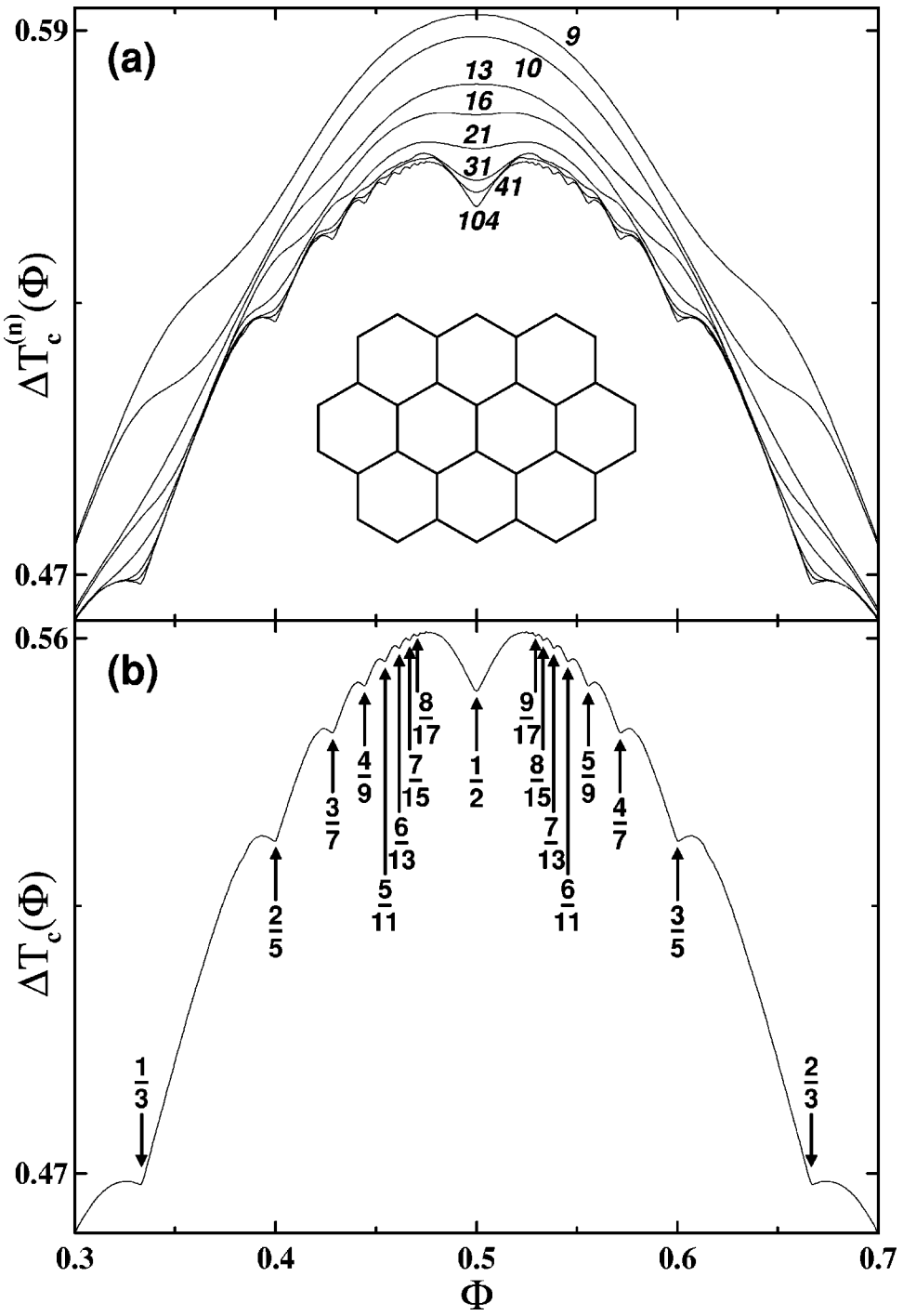

FIG. 4. Superconducting transition temperature for the honeycomb network as a continuous function of the applied magnetic field: $\Delta T_c^{(n)}(\Phi) = T_c(0) - T_c^{(n)}(\Phi)$ vs Φ, the magnetic flux through an elementary hexagonal cell. In (a) we show the superconducting-normal phase boundaries computed from the truncated Hamiltonians $H^{(n)}$ for Φ in the range between 0.3 and 0.7. We omit the parts of $\Delta T_c^{(n)}(\Phi)$ for $\Phi \in [0, 0.3]$ and $[0.7, 1]$ since there are no interesting features in these portions of $\Delta T_c^{(n)}(\Phi)$. From top to bottom, the orders of truncation are $n=9$ (top curve), 10, 13, 16, 21, 31, 41, and 104. Note the development of fine structures and cusps. The convergence is monotonic. We believe that $\Delta T_c^{(104)}(\Phi)$ has achieved close convergence to the infinite system size $\Delta T_c(\Phi)$. The inset schematically depicts a honeycomb lattice. In (b), we plot $\Delta T_c(\Phi)$ for $\Phi \in [0.3, 0.7]$ and label the values of the magnetic flux where observable cusps and dips occur. They include $\Phi = 1/3$, 2/5, 3/7, 4/9, 5/11, 6/13, 7/15, 8/17, 1/2, 9/17, 8/15, 7/13, 6/11, 5/9, 4/7, 3/5, and 2/3. Here $\Delta T_c(\Phi) \equiv \Delta T_c^{(104)}(\Phi) = T_c(0) - T_c^{(104)}(\Phi)$, our calculated highest-order approximant.

and

$$\Phi = \frac{m+1}{2m+1}$$

with $m \geqslant 1$. Our computed phase boundary compares well with the observed cusps present in experiments.[20,21]

VII. TRIANGULAR LATTICE

For the triangular lattice, we denote the lattice path integrals by t_l. In other words, t_l is the exact sum of the phase factors of all l-step closed paths on the triangular lattice. In this section, $\phi/2\pi$ corresponds to the magnetic flux through an elementary triangular plaquette, i.e.,

$$\frac{\phi}{2\pi} = \frac{\sqrt{3}c^2 B}{4\Phi_0}.$$

The results for t_2 through t_{10} are

$$t_2 = 6,$$

$$t_3 = 12\cos\phi,$$

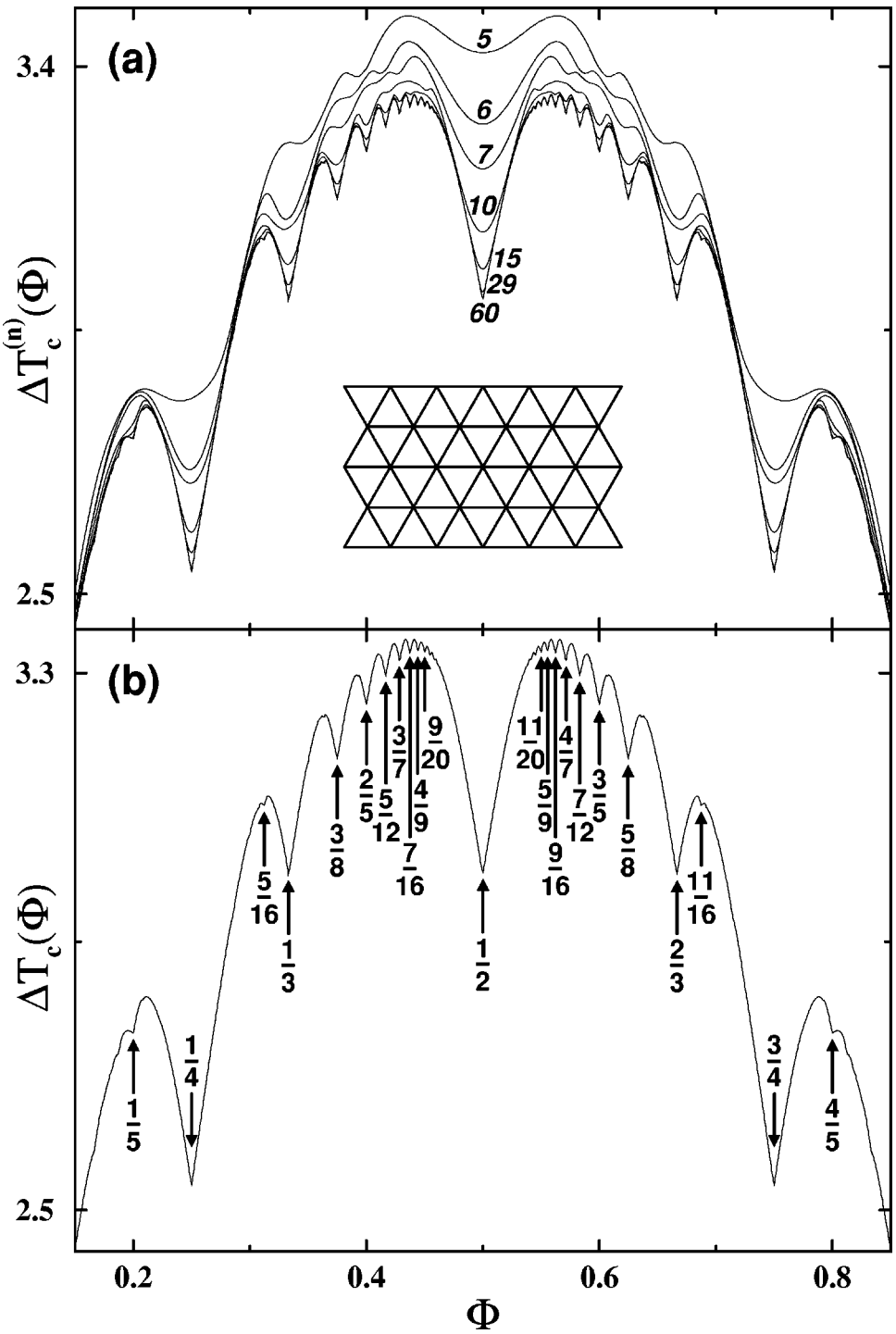

FIG. 5. Superconducting transition temperature for the triangular network as a continuous function of the applied magnetic field: $\Delta T_c^{(n)}(\Phi)=T_c(0)-T_c^{(n)}(\Phi)$ vs Φ, the magnetic flux through an elementary triangular cell. In (a) we show the superconducting-normal phase boundaries computed from the truncated Hamiltonians $H^{(n)}$ for Φ in the range between 0.15 and 0.85. We omit the parts of $\Delta T_c^{(n)}(\Phi)$ for $\Phi \in [0, 0.15]$ and $[0.85, 1]$ since there are no interesting features in these portions of $\Delta T_c^{(n)}(\Phi)$. From top to bottom, the orders of truncation are $n=5$ (top curve), 6, 7, 10, 15, 29, and 60. Note the development of fine structures and cusps. The convergence is monotonic and rapid. Note also that the closeness between the curves for $\Delta T_c^{(29)}(\Phi)$ and $\Delta T_c^{(60)}(\Phi)$ implies that $\Delta T_c^{(60)}(\Phi)$ has achieved close convergence to the infinite system size $\Delta T_c(\Phi)$. The inset schematically depicts a triangular lattice. In (b), we plot $\Delta T_c(\Phi)$ for $\Phi \in [0.15, 0.85]$, our calculated highest-order approximation to $\Delta T_c(\Phi)$, and label the values of the magnetic flux where observable cusps and dips occur. They include $\Phi = 1/5$, 1/4, 5/16, 1/3, 3/8, 2/5, 5/12, 3/7, 7/16, 4/9, 9/20, 1/2, 11/20, 5/9, 9/16, 4/7, 7/12, 3/5, 5/8, 2/3, 11/16, 3/4, and 4/5. Here $\Delta T_c(\Phi) \equiv \Delta T_c^{(60)}(\Phi) = T_c(0) - T_c^{(60)}(\Phi)$, our calculated highest-order approximant.

$$t_4 = 66 + 24\cos 2\phi,$$

$$t_5 = 300\cos\phi + 60\cos 3\phi,$$

$$t_6 = 1020 + 840\cos 2\phi + 168\cos 4\phi + 12\cos 6\phi,$$

$$t_7 = 6888\cos\phi + 2604\cos 3\phi + 504\cos 5\phi + 84\cos 7\phi,$$

$$t_8 = 19890 + 23904\cos 2\phi + 8568\cos 4\phi + 1968\cos 6\phi + 432\cos 8\phi + 48\cos 10\phi,$$

$$t_9 = 164124\cos\phi + 85944\cos 3\phi + 29628\cos 5\phi + 8496\cos 7\phi + 1980\cos 9\phi + 432\cos 11\phi + 36\cos 13\phi,$$

$$t_{10} = 449976 + 654840\cos 2\phi + 317940\cos 4\phi + 114360\cos 6\phi + 37560\cos 8\phi + 10380\cos 10\phi + 2700\cos 12\phi + 540\cos 14\phi + 60\cos 16\phi.$$

Here we explain how the first few lattice path integrals are

obtained. Since there is no path of one step for returning an electron to its initial site, t_1 is always equal to zero. There are six closed paths of two steps each [retracing each other on one bond $(\cdot\leftrightarrow)$, where the dot $\cdot$ indicates the initial site], thus

$$t_2 = 6\cdot\leftrightarrow = 6e^{i0\phi} = 6 = z,$$

where z is the coordination number of the lattice.

There are 12 three-step closed paths enclosing a triangular cell [three counterclockwise $(\cdot\,\vec{\nabla})$, and three clockwise $(\cdot\,\vec{\nabla})$]. Thus

$$t_3 = 6\cdot\vec{\nabla} + 6\cdot\vec{\nabla} = 6e^{i\phi} + 6e^{-i\phi} = 12\cos\phi.$$

There are 66 closed paths of four steps each enclosing zero flux each: six retracing twice on one bond $(\overset{\leftrightarrow}{\cdot\leftrightarrow})$, 30 starting from a site connecting two adjacent bonds and retracing once on each bond $(\leftrightarrow\cdot\leftrightarrow)$, and 30 moving two bonds away and then two bonds back to the original site $(\overset{\leftarrow\ \leftarrow}{\cdot\rightarrow\rightarrow})$. Since all of them enclose no area (i.e., no flux), then

$$t_4^{\text{no flux}} = 6\,\overset{\leftrightarrow}{\cdot\leftrightarrow} + 30\leftrightarrow\cdot\leftrightarrow + 30\,\overset{\leftarrow\ \leftarrow}{\cdot\rightarrow\rightarrow} = 66.$$

Among the four-step closed paths, 24 of them enclose adjacent cells enclosing two triangles (12 counterclockwise and 12 clockwise) and contribute

$$t_4^{\text{two cells only}} = 12e^{2i\phi} + 12e^{-2i\phi} = 24\cos 2\phi$$

to t_4. Thus, it follows that $t_4 = 66 + 24\cos 2\phi$.

Note that t_{2l} (t_{2l+1}) consist of only even (odd) harmonics of the flux. We have computed the lattice path integrals for the triangular lattice up to t_{119}, which are obtained by exactly summing up $\sim 10^{90}$ closed paths. These calculated t_l's have enabled us to obtain the phase boundary up to $T_c^{(60)}(\phi)$.

By using the calculated results for t_l, the parameters a_n and b_n, and subsequently the corresponding truncated Hamiltonians $H^{(n)}$, can be obtained. For instance, the second-order truncation of the Hamiltonian is

$$H^{(2)} = \begin{bmatrix} 0 & \sqrt{6} \\ \sqrt{6} & 2\cos\phi \end{bmatrix}.$$

Its corresponding top eigenvalue is

$$T_c^{(2)}(\phi) = \cos\phi + \sqrt{6 + \cos^2\phi}.$$

The third-order truncation of the Hamiltonian is

$$H^{(3)} = \begin{bmatrix} 0 & \sqrt{6} & 0 \\ \sqrt{6} & 2\cos\phi & \sqrt{1+4\cos^2\phi} \\ 0 & \sqrt{1+4\cos^2\phi} & \dfrac{-8\cos\phi + 16\cos^3\phi}{1+4\cos^2\phi} \end{bmatrix}.$$

Its corresponding top eigenvalue $T_c^{(3)}(\phi)$ can also be obtained analytically.

In Fig. 5, we show the superconducting transition temperatures, $\Delta T_c^{(n)}(\Phi) = T_c(0) - T_c^{(n)}(\Phi)$, as functions of $\Phi \equiv \phi/2\pi$ for various n for the triangular network obtained from the truncated Hamiltonians $H^{(n)}$. Here $T_c(0)$ equals 6, which is the largest eigenvalue of tight-binding electrons confined on the triangular lattice in the absence of a magnetic field. The following physical picture is clear from those plots: as the order of approximation is increased, more geometrical information of the lattice is included in the interference treatment and more fine structures are resolved.

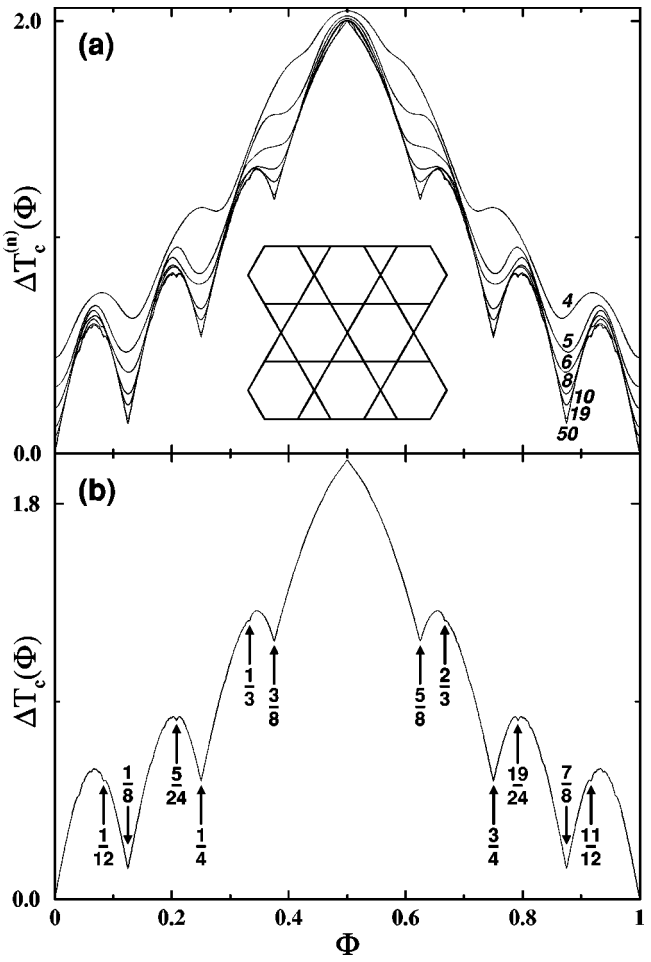

FIG. 6. Superconducting transition temperature for the kagomé network as a function of the applied magnetic field: $\Delta T_c^{(n)}(\Phi) = T_c(0) - T_c^{(n)}(\Phi)$ vs Φ, the magnetic flux through an elementary triangular cell. In (a) we show the superconducting-normal phase boundaries computed from the truncated Hamiltonians $H^{(n)}$ for Φ in the range between 0 and 1. From top to bottom, the orders of truncation are $n=4$ (top curve), 5, 6, 8, 10, 19, and 50. Note the development of fine structures and cusps. The convergence is monotonic. Note also that the closeness between the curves for $\Delta T_c^{(19)}(\Phi)$ and $\Delta T_c^{(50)}(\Phi)$ implies that $\Delta T_c^{(50)}(\Phi)$ has achieved close convergence to the infinite system size $\Delta T_c(\Phi)$. The inset schematically depicts a kagomé lattice. In (b), we plot $\Delta T_c(\Phi)$ for $\Phi \in [0,1]$ and label the values of the magnetic flux where observable cusps and dips occur. They include $\Phi = 1/12$, 1/8, 4/25, 1/4, 1/3, 3/8, 5/8, 2/3, 3/4, 19/24, 7/8 and 11/12. Here $\Delta T_c(\Phi) \equiv \Delta T_c^{(50)}(\Phi) = T_c(0) - T_c^{(50)}(\Phi)$, our calculated highest-order approximant. Note the absence of the cusp at $\Phi = 1/2$. This distinct feature is in sharp contrast to the cases for square, honeycomb, and triangular networks.

Our highest-order approximant, $T_c^{(60)}(\Phi)$ has closely reached the infinite- system- size limit $\Delta T_c(\Phi)$. The flux values where the cusps occurred have also been labeled. In general, besides the cusps at $\Phi=1/2$, 1/5, 4/5, 5/16, 11/16, there are cusps and dips at

$$\Phi=\frac{m}{2m+2}$$

and

$$\Phi=\frac{m+2}{2m+2},$$

with $m\geqslant 1$.

VIII. KAGOMÉ LATTICE

Our computed phase boundary compares well with the observed cusps present in a series of interesting experiments.[20,21]

For the kagomé lattice,[15,20–24] we denote the lattice path integrals by k_l. In other words, k_l is the exact sum of the phase factors of all l-step closed paths on the kagomé lattice. Here $\phi/2\pi$ corresponds to the magnetic flux through an elementary triangular plaquette, i.e.,

$$\frac{\phi}{2\pi}=\frac{\sqrt{3}c^2B}{4\Phi_0}.$$

The results for k_2 through k_{11} are

$$k_2=4,$$

$$k_3=4\cos\phi,$$

$$k_4=28,$$

$$k_5=60\cos\phi,$$

$$k_6=244+16\cos 2\phi+4\cos 6\phi,$$

$$k_7=756\cos\phi+28\cos 7\phi,$$

$$k_8=2412+416\cos 2\phi+96\cos 6\phi+80\cos 8\phi,$$

$$k_9=9216\cos\phi+76\cos 3\phi+36\cos 5\phi+756\cos 7\phi+120\cos 9\phi,$$

$$k_{10}=25804+7560\cos 2\phi+1860\cos 6\phi+2480\cos 8\phi+100\cos 10\phi+20\cos 14\phi,$$

$$k_{11}=112420\cos\phi+2816\cos 3\phi+1276\cos 5\phi+14608\cos 7\phi+4400\cos 9\phi+44\cos 11\phi+44\cos 13\phi+176\cos 15\phi.$$

Note that k_{2l} (k_{2l+1}) comprise only even (odd) harmonics of the flux. We have computed the lattice path integrals for the kagomé lattice up to t_{99}, which are obtained by exactly sum-

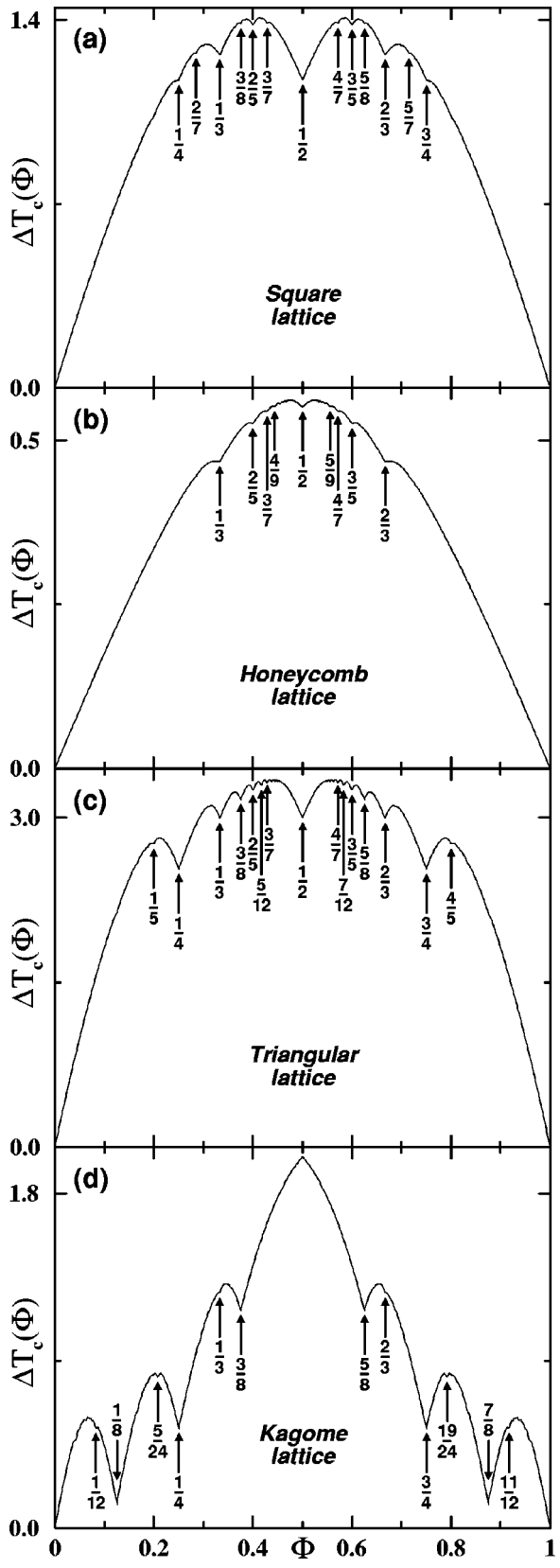

FIG. 7. $\Delta T_c(\Phi)$'s as functions of Φ between 0 and 1 for the superconducting square, honeycomb, triangular, and kagomé networks, respectively, from (a) to (d). Notice the difference in the vertical scales.

ming up $\sim 10^{58}$ closed paths. These calculated k_l's have enabled us to obtain the phase boundary up to $T_c^{(50)}(\phi)$.

By using the calculated results for k_l, the parameters a_n and b_n, and subsequently the corresponding truncated Hamiltonians $H^{(n)}$, can be obtained. For instance, the second-order truncation of the Hamiltonian is

$$H^{(2)}=\begin{bmatrix} 0 & 2 \\ 2 & \cos\phi \end{bmatrix}.$$

Its corresponding top eigenvalue is

$$T_c^{(2)}(\phi)=\frac{1}{2}(\cos\phi+\sqrt{16+\cos^2\phi}).$$

The third-order truncation of the Hamiltonian is

$$H^{(3)}=\begin{bmatrix} 0 & 2 & 0 \\ 2 & \cos\phi & \sqrt{3-\cos^2\phi} \\ 0 & \sqrt{3-\cos^2\phi} & \dfrac{\cos\phi+\cos^3\phi}{3-\cos^2\phi} \end{bmatrix}.$$

Its corresponding top eigenvalue $T_c^{(3)}(\phi)$ can also be obtained analytically.

In Fig. 6, we show the superconducting transition temperatures $\Delta T_c^{(n)}(\Phi)=T_c(0)-T_c^{(n)}(\Phi)$ as functions of $\Phi \equiv \phi/2\pi$ for various n for the kagomé network obtained from the truncated Hamiltonians $H^{(n)}$. Here $T_c(0)$ equals 4 which is the largest eigenvalue of tight-binding electrons confined on the kagom e lattice in the absence of the magnetic field. It is seen that as the order of the approximation is increased, more geometrical information of the lattice is included in the interference treatment and more fine structures are resolved. We emphasize that our highest-order approximant $T_c^{(50)}(\Phi)$ has closely reached the infinite-system-size limit $\Delta T_c(\Phi)$. The flux values where the cusps and dips occurred have also been labeled. Our computed phase boundary compares well with the observed cusps present in a series of interesting experiments.[20,21] See also the systematic calculations in Ref. 22.

IX. DISCUSSION

In the following, we discuss the general trends in the approximants for these phase diagrams presented in the above sections.

A. Comparison of the structure in the phase boundaries

In the lower-order approximants, the first noticeable development in the phase boundaries of square, honeycomb, and triangular lattices is the formation of dips when the flux per elementary plaquette is equal to $m\Phi_0/2$, where m is an integer. When the order of approximation is increased, the dips at $\Phi=1/2$ become sharper and at the same time more fine structures (other local minima) begin to emerge. Eventually, the dips at various different flux values become cusps.

It is interesting to notice that, among these three lattices, the development of the cusps is most rapid for the triangular case while the honeycomb is the slowest. This difference originates from the fact that for identical lengths, lattice path integrals for the triangular lattice contain the richest *quantum interference* effects because the number of paths and the areas they enclose are both the largest. For the kagomé network, the rapid development of cusps at

$$\Phi^{\text{kagomé}}=\frac{1}{8},\frac{1}{4},\frac{3}{8},\frac{5}{8},\frac{3}{4},\frac{7}{8}$$

can be seen from lower-order approximants. For an additional discussion of the kagomé case, see Ref. 15. For extensions of these techniques to other problems, see Ref. 25.

In general, the resulting phase diagrams—with the occurrence of cusps and dips at different sets of flux values—are a direct consequence of the geometries of the lattices, which is explicitly reflected in the corresponding expressions of the lattice path integrals. We stress that our evaluation of the lattice path integrals to extremely long lengths has enabled our calculated $T_c(B)$ to achieve close convergence to the infinite system size. Indeed, for $n \simeq 10$, important features in the phase boundaries of square, triangular, and kagom e networks are well developed.

Finally, in order to facilitate a comparison between the different phase boundaries, in Fig. 7 we plot $\Delta T_c(\Phi)$ as a function of Φ for the square, honeycomb, triangular, and kagomé superconducting networks. Here the $\Delta T_c(\Phi)$'s are taken from their respective highest-order approximants and Φ is the flux through their respective elementary cells as discussed in the previous sections. Here we omit the subscripts indicating the order of approximation. The values of the magnetic flux corresponding to a number of prominent cusps and dips are also labeled.

B. Comparison of the phase boundaries of the single-loop and lattice cases

From Figs. 1 and 7(a)–7(c), we can readily see the differences between the phase boundaries of a single superconducting cell and its corresponding superconducting network. For both cases, ΔT_c varies periodically with the magnetic flux through a single elementary cell and has the same period Φ_0 of oscillation. We now focus on $\Delta T_c(\Phi)$ for Φ in the interval between 0 and 1. $\Delta T_c(\Phi)$ is symmetric around $\Phi=1/2$. However, there are many distinct features between ΔT_c of a single cell and that of a network. These differences are due to long-range correlations of the many-loop effect present in the lattice. For a single superconducting cell, $\Delta T_c(\Phi)$ increases monotonically from $\Phi=0$ to $\Phi=1/2$ and decreases monotonically from $\Phi=1/2$ to $\Phi=1$. The maximum at $\Phi=1/2$ exhibits a sharp peak. Indeed, the overall shape of $\Delta T_c(\Phi)$ resembles the combination of two identical half parabolas, both reaching their maximum at $\Phi=1/2$. On the contrary, the overall shape of $\Delta T_c(\Phi)$ for the corresponding superconducting networks looks like downward parabolas with many local cusps between $\Phi=0$ and $\Phi=1$. The most prominent cusps are located at $\Phi=1/2$. The positions of other cusps and dips depend on the underlying lattice types of the networks.

C. Differences between our approach and the traditional moments and Lanczos methods

In electronic structure calculations there is a method to compute the density of states called the moments method. This is similar to our approach in the sense that μ_l can be interpreted as the moments $\langle \Psi_i | H^l | \Psi_i \rangle$. However, there are several important differences between the standard ''moments method'' and our problem. The typical use of the moments method (i) focuses on computation of the electronic density of states (instead of superconducting T_c's), (ii) is totally numerical (instead of mostly analytical), (iii) is done at zero magnetic field (instead of obtaining expressions with an explicit field dependence), (iv) does not focus on the explicit computation of lattice path integrals, and (v) does not study the physical effects of quantum interference (which is at the heart of our calculation and physical interpretation). In conclusion, the traditional use of the moments method in solid-state physics is significantly different from the approach and problem studied here.

Another way to diagonalize Hamiltonians is called the Lanczos method. This method directly obtains the tridiagonal form, without computing the moments, and thus differs in a significant way from the approach used here (where the explicit computation of the moments is one of our goals, since they can be used for other electronic property calculations). Furthermore, it is not convenient to use the standard Lanczos method in our particular problem because it is extremely difficult to directly derive the parameters and the states of the iterative tridiagonalization procedure. This is so because of the presence of the magnetic field. On the other hand, the moments method provides standard procedures to diagonalize a matrix after the moments are computed.

D. Commensurability and other matching effects

An essential physics issue in this problem is *commensurability*. Another one is *quantum interference*—due to the motion of electrons in multiconnected geometries. This section briefly overviews related systems where commensurability and matching effects (due to externally applied magnetic fields) play an important role. The first example will be flux pinning.

Flux pinning in type-II superconductors is of both technological and scientific interest. While most experiments focus on the effects of random pinning distributions, some investigations have been carried out on periodic arrays of pinning sites.[1,26] These find striking peaks in the magnetization[27] and critical current J_c. These peaks are believed to arise from the greatly enhanced pinning that occurs when parts of the vortex lattice (VL) become commensurate with (i.e., match) the underlying periodic array of pinning sites. Under such conditions, high-stability vortex configurations are produced which persist under an increasing current or external field.

Other important vortex matching effects have also recently been observed in a variety of different superconducting systems,[28–30] including long Josephson junctions with periodically spaced grooves,[29] superconducting networks,[26] and the matching of the VL to the crystal structure of $YBa_2Cu_3O_7$ due to intrinsic pinning.[30]

Matching effects between a vortex lattice and periodic pinning arrays produce a rich variety of effects.[31] The dynamics observed in these systems is quite different from the one found for random arrays of pinning sites (see, e.g., Ref. 32 and references therein).

Nonsuperconducting systems also exhibit magnetic-field-tuned matching effects, notably in relation to electron motion in periodic structures where unusual behaviors arise due to the incommensurability of the magnetic length with the lattice spacing. A recent example of these is provided by the anomalous Hall plateaus of ''electron pinball''[33] orbits scattering from a regular array of antidots.

Commensurate effects also play central roles in many other areas of physics, including plasmas, nonlinear dynamics,[34] the growth of crystal surfaces, domain walls in incommensurate solids, quasicrystals, and Wigner crystals, as well as spin and charge density waves. The next section discusses in some detail an example in nonlinear dynamics (which is virtually unknown in the solid-state literature) that produces a fractal phase boundary which is strikingly similar to the one measured for square superconducting networks—because both are determined by commensurability effects.

E. Kagomé-pinned vortices: ''Correlated melting'' and cooperative ring excitations for doubly degenerate ground states

Notice that the fluxoid configurations for $f=1/2$ for the superconducting networks (e.g., Fig. 3 of Xiao *et al.*, in the companion article[20]) has two ground states that correspond to the two degenerate ground states of the second matching field of vortices in type-II superconductors with a kagomé periodic array of pinning sites. The latter has been systematically studied in Ref. 24.

The kagomé pinning potential at the second matching field shows novel and interesting dynamics as a function of temperature,[24] including a phase with rotating vortex triangles caged by kagomé hexagons (''cooperative ring elementary excitations''), and there is geometric frustration for $T \to 0$ with a doubly degenerate ground state. At finite temperatures, the three vortices inside the kagom e hexagon can move and rotate by 60°. This is done cooperatively by the three vortices. They motion is similar to the ''cooperative ring exchange'' motion proposed by Feynman for elementary excitations in helium 4.

In other words, for the second matching field for the kagomé pinning lattice, the elementary excitation of the three interstitial vortices is a 60° rotation, rotating as a cooperative ring. These types of collective or correlated cooperative ring exchanges have also been studied in the context of the quantum Hall effect.

For increasing temperatures, a novel type of melting[24] appears, which is not treated here using our path-integral approach, but can be studied using other techniques.[24] This can be described as ''correlated melting'' in the sense that the ''triangle'' or ''loop'' first melts in the angular coordinate, while the radial coordinate does not melt until much higher temperatures are reached. The elementary excitations are the thermal analog of certain types of *squeezed states* (where

fluctuations strongly affect a coordinate and less the other coordinate). They are also analogs of the *rotational isomers* or ''comformations'' that are often found in molecules, where three atoms and molecules can cooperatively oscillate back and forth between two degenerate ground states.

This type of ''controlled melting'' or ''correlated melting''[24] of the particles inside a potential energy trap could also be visualized with a colloidal suspension surrounded by six pinned (e.g., by laser tweezers) charged particles. This type of ''vortex-analog'' experiment is easier to visualize (e.g., via optical microscope) than using vortices. Still, Lorentz microscopy techniques[35] could directly image such motions in the vortex case.

F. Fractal phase boundaries and fractal boundaries of basins of attraction

There is a striking similarity between two apparently unrelated problems: the superconducting-normal phase boundary of a square superconducting network (our Fig. 2) and the fractal phase boundary (see, for instance, Fig. 6.26 of Ref. 34) of basins of attraction of a dynamical systems map studied last century by Weierstrass and generalized much later by Hardy in 1916.

The reason for this very interesting similarity among these two apparently unrelated problems is because the commensurability condition dominates both problems and produces a large dip at 1/2 and smaller dips at 1/4, 1/3, 2/5, etc., as discussed previously in this work.

It is interesting to summarize how to obtain the Weierstrass fractal boundary of two basins of attraction.[34] Consider the dynamical map M,

$$(x_{k+1},\theta_{k+1})=M(x_k,\theta_k),$$

defined by

$$x_{k+1}=\lambda x_k+\cos\theta_k$$

and

$$\theta_{k+1}=2\theta_k(\mathrm{mod}\,2\pi).$$

When $1<\lambda<2$, the map M has two attractors, at $x=\pm\infty$. Indeed, since the eigenvalues of the Jacobian matrix are 2 and $\lambda>1$, there are no finite attractors. Therefore,

$$M^N(x_0,\theta_0)=(x_N,\theta_N\mathrm{mod}(2\pi)),$$

and x_N tends to either $+\infty$ or $-\infty$ as $N\to\infty$, except for the unstable boundary set

$$x=f(\theta),$$

for which x_N remains finite.

To locate this $x=f(\theta)$ boundary set, first note that

$$\theta_k=2^k\theta_0(\mathrm{mod}\,2\pi).$$

The map is noninvertible since it is two to one. However, any x_N can be selected and then find one orbit that ends at (x_N,θ_N), by using the above θ_k and taking

$$x_{k-1}=\lambda^{-1}[x_k-\cos(2^{k-1}\theta_0)].$$

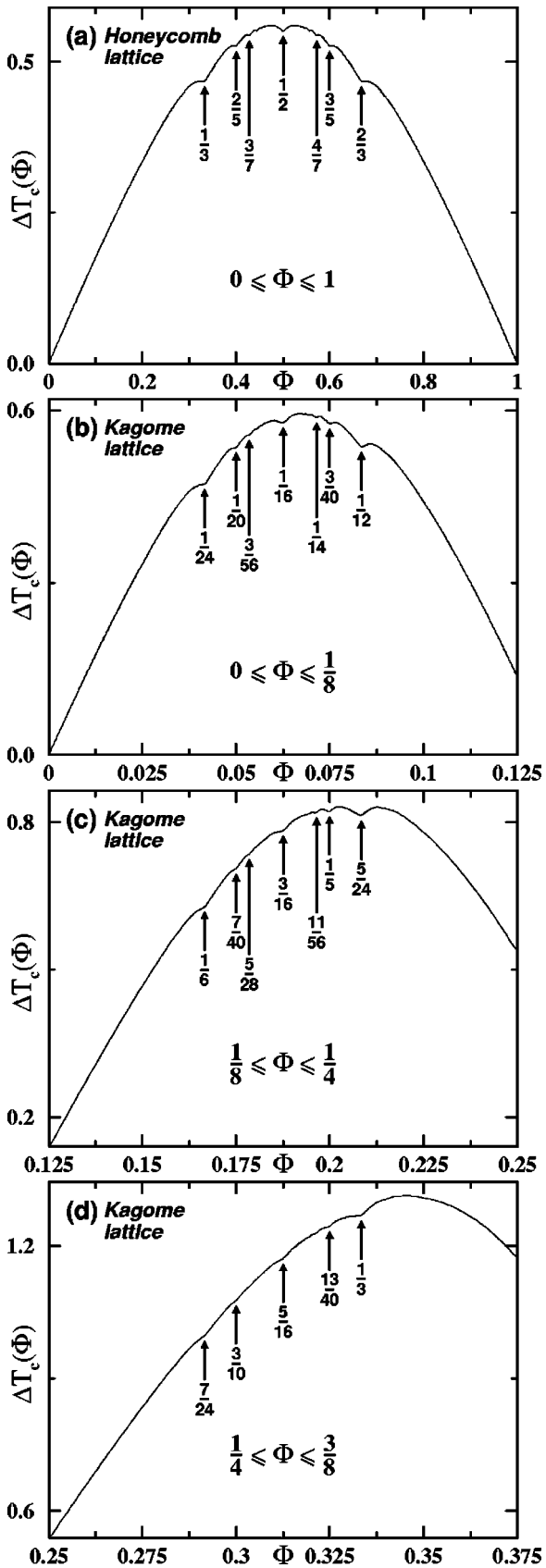

FIG. 8. $\Delta T_c(\Phi)$ vs Φ. (a) is for the superconducting honeycomb network for Φ in the range [0,1]. (b), (c), and (d) are for the superconducting kagomé network for Φ, respectively, in the ranges [0, 1/8], [1/8, 1/4], and [1/4, 3/8].

For a given (x_N, θ_N), this orbit starts at

$$x_0 = \lambda^{-1} x_N - \sum_{l=0}^{N-1} \lambda^{-l-1} \cos(2^l \theta_0).$$

Those (x_0, θ_0) such that x_N is finite as $N \to \infty$, define the boundary $x = f(\theta)$ between the two basins. Therefore the relation between these x and θ is given by

$$x = -\sum_{l=0}^{\infty} \lambda^{-l-1} \cos(2^l \theta_0) \equiv f(\theta). \tag{8}$$

This sum obviously converges, since $\lambda > 1$. However, its derivative

$$\frac{df(\theta)}{d\theta} = \frac{1}{2} \sum_{l=0}^{\infty} \left(\frac{2}{\lambda}\right)^{l+1} \sin(2^l \theta)$$

diverges, since $\lambda < 2$. Thus, $f(\theta)$ is nondifferentiable. Like our superconducting-normal phase boundary, it has a large cusp at 1/2 and smaller cusps at 1/3, 1/4, 2/5, etc. Moreover, it is also symmetric around 1/2, and it strongly resembles the $\Delta T_c(\Phi)$ [obtained near $R(T) = 0$] for a square lattice. Indeed, $\Delta T_c(\Phi)$ corresponds to x, Φ to θ, and λ corresponds to how close the measurement is done to the critical point.

When λ approaches 2 from below, the fractal dimension d_c approaches 1 (mean-field limit, when the measurement is not done close to the critical point). When λ approaches 1 from above, the fractal dimension d_c approaches 2, from below.

The fractal dimension of $x = f(\theta)$, Eq. (8) above, is

$$d_c = 2 - \frac{\ln \lambda}{\ln 2}.$$

The precise value of d_c depends on the value of λ. Recall that $1 < \lambda < 2$. For λ sligthly less than 2, the fractal dimension d_c approaches 1, and the dips are not pronounced. This is similar to the superconducting-normal phase boundaries measured not too close to T_c [e.g., at midpoint drop for the $R(T)$ plot]. When the phase boundary is measured very near T_c [when $R(T)$ is very near zero], the number of discernible dips grows and they become very sharp (see, e.g., Figs. 10 and 11 of Ref. 14). This would corespond to λ slightly above 1; thus, the fractal dimension d_c of the Weierstrass function would be closer to 2 (i.e., a ''rougher'' or ''spikier'' curve).

Indeed, Ref. 14 solved for $\Delta T_c(\Phi)$ beyond the mean-field theory approximation, obtaining a phase boundary similar to the Weierstrass function for λ slightly above 1, and d_c near 2. That superconducting-normal phase boundary in Ref. 14 has very sharp cusps and dips, and (like the Weierstrass function) it is a *phase boundary between attractors*. The map for the superconducting networks is obtained from a real-space renormalization-group technique. The mean-field limit provides a smoother phase boundary with λ closer to 1. The real-space bond decimation scheme of Ref. 14 also favors fluxes of the form $\Phi = 2^l \Phi_0$. This is clear from the way the real-space renormalization-group scheme is constructed, where four elementary cells are ''blocked away'' into a larger cell with new renormalized effective couplings. Four of these supercells are then blocked away into another, larger cell, enclosing 16 elementary cells (or 4 supercells). This process is *iterated*, until the renormalization-group (RG) procedure coverges (at the phase boundary) or diverges to fixed points located away from the fixed point (e.g., $+\infty$). This (beyond-mean-field) RG iteration[14] and the Weierstrass iteration involve very similar types of maps and this generates the strikingly similar curves.

In summary, the Weierstrass function and our real-space renormalization-group approach[14] both produce phase boundaries which are strikingly similar. In particular, both are nondifferetiable, symmetric around 1/2, and have a very similar hierarchy of cusps.

X. COMPARISON OF THE PHASE BOUNDARIES OF SUPERCONDUCTING HONEYCOMB AND KAGOMÉ NETWORKS

Here we discuss an interesting relation between the phase boundaries of superconducting honeycomb and kagomé networks which is due to the *geometrical* arrangements of these two types of lattices. Indeed, and as kindly pointed out to us by Xiao and Chaikin (e.g., see Ref. 20), it is very useful to focus on the region $0 \leqslant \Phi \leqslant 1$ for the honeycomb network and the region $0 \leqslant \Phi \leqslant 1/8$ for the kagomé network.

As shown in Figs. 8(a)–8(d), though the overall shapes of the phase diagrams are different, there is a one-to-one correspondence between the dips in the honeycomb $\Delta T_c(\Phi)$ for Φ, the flux through an elementary hexagon, in the range $[0,1]$ and those in the kagomé $\Delta T_c(\Phi)$ for Φ, the flux through an elementary triangle, in the ranges $[0,1/8]$, $[1/8,1/4]$, and $[1/4,3/8]$. To state this relationship more precisely, let $\{p/q\}$ be the set of flux values characterizing a number of dips in the $\Delta T_c(\Phi)$ curve for the honeycomb network. For instance, as labeled in (a),

$$\{p/q\} = 1/3,\ 2/5,\ 3/7,\ 1/2,\ 4/7,\ 3/5,\ 2/3.$$

It is observed that the corresponding set of flux values for the dips to occur in the kagomé $\Delta T_c(\Phi)$ curve would be $\{p/8q\}$ when Φ lies in the range $[0,1/8]$. Similarly, the corresponding sets read, respectively,

$$\Phi = \left\{ \frac{1}{8} + \frac{p}{8q} = \frac{p+q}{8q} \right\}$$

for $\Phi \in [1/8,\ 1/4]$ and

$$\Phi = \left\{ \frac{1}{4} + \frac{p}{8q} = \frac{p+2q}{8q} \right\}$$

for $\Phi \in [1/4,\ 3/8]$. Note that for Φ in the range $[1/4,\ 3/8]$, the dips in the $\Delta T_c(\Phi)$ curve become less evident: only five flux values are observed and labeled. The location and magnitude of the dips found here are consistent with recent very interesting experiments by the NEC and Princeton groups.[20,21]

Recall that kagomé magnets are known to have degenerate ground states (see, e.g., Ref. 23 and references therein). Likewise, for superconducting kagomé networks at half fill-

ing, there are several possible ways to arrange fluxes, producing a large degeneracy in the $T=0$ ground state.[15] This issue of degeneracy between two states has been systematically studied as a function of temperature via computer simulations on superconducting samples with a kagomé-arranged periodic array of pinning sites.[24] The second matching field in this system has two fluxons per pinning site. This corresponds to the $f=1/2$ state in the kagom e superconducting network. For this value of the externally applied magnetic field, every hexagon has two states (with entropy $k_B \ln 2$). N hexagons would have 2^N states and a very large entropy

$$S^{(N \text{ hexagons})} \sim N k_B \ln 2 .$$

Thus, at the second matching field, superconductors with either a kagomé or an hexagonal array of pinning sites both have ''low-energy states'' with a very large degeneracy and a huge (low-T) entropy. Thus, when cooling from high temperatures, it is difficult to find a unique $T=0$ ground state. Transport measurements and mean-field theory perhaps might not be sufficient to fully elucidate the role of bistability and degeneracy in this system. In order to explore this scenario in a more systematic manner, different tools (e.g., flux imaging techniques[35] and computer simulations[24] of vortex dynamics on kagomé lattices) might be needed.

After this work was completed, we became aware of a very interesting relevant work by Park and Huse in Ref. 22. Using Ginzburg-Landau theory, they study superconducting kagomé wire networks in a transverse magnetic field when the magnetic flux through an elementary triangle is a half of a flux quantum. They calculate the helicity moduli of each phase to estimate the Kosterlitz-Thouless (KT) transition temperatures. At the KT temperatures, they estimate the barriers to move vortices and the effects that lift the large degeneracy in the possible flux patterns.

XI. SUMMARY

In conclusion, we present a detailed study of the mean-field superconducting-normal phase boundaries of superconducting square, honeycomb, triangular, and kagomé networks. Our investigations are based on studying the quantum interference effects arising from the summation of all the closed paths the electron can take on the underlying lattices. Other problems[25] have also been studied in terms of the quantum interference of electron paths. We then adopt a systematic approximation scheme to obtain the spectral edges of the corresponding eigenvalue problems, and relate the features in the phase boundaries with the geometry of the underlying lattice being explored by the moving electrons. When the electrons are allowed to explore a sizable region of the network, our calculations have quickly reached very close convergence to the infinite-system size-results. There are two particular advantageous aspects of this approach. First, it enables us to evaluate the superconducting transition temperature as a *continuous* function of the applied magnetic field. Second, it enables us to achieve a step-by-step derivation of the *physical origin* of the many structures in the phase diagrams—in terms of the regions of the lattice explored by the electrons. In particular, the larger the region of the network the electrons can explore (and thus more paths are available for the electron), the finer structure appears in the phase boundary and the sharper the cusps become. We find many new interesting features in these phase diagrams, which compare well with experiments.

ACKNOWLEDGMENTS

We thank Paul M. Chaikin and Yi Xiao for helpful conversations and for sending us their experimental results. Y.-L.L. acknowledges support at West Virginia University from the National Science Foundation (NSF) under Grant No. DMR-91-20333. F.N. acknowledges support from NSF Grant No. EIA-0130383 and from the Frontier Research System, The Institute of Physical and Chemical Research (RIKEN), Saitama, Japan. F.N. also acknowledges B. Janko for his hospitality during a visit at the Materials Science Division of Argonne National Laboratory, partially supported by DOE Grant No. W-31-109-ENG-38. Partial support has been also provided by the University of Michigan Center for Theoretical Physics and the Center for the Study of Complex Systems.

*Corresponding author. Permanent address: The University of Michigan, Ann Arbor, MI 48109-1120; electronic address: nori@umich.edu

[1] For a recent and very extensive review, see R.S. Newrock, C.J. Lobb, U. Geigenmuller, and M. Octavio, Solid State Phys. **54**, 263 (2000); For previous overviews, see, e.g., B. Pannetier, J. Chaussy, and R. Rammal, Jpn. J. Appl. Phys., Part 1 **26**, 1994 (1987); P. Martinoli, *ibid.* **26**, Suppl. 26-3, 1989 (1987); C.J. Lobb, Physica B **126**, 319 (1984); and the many articles in the issue on *Coherence in superconducting networks*, edited by J.E. Mooij and G.B.J. Schön [*ibid.* **152B**, 1 (1988)]. Early work on superconducting wires appears in B. Pannetier, J. Chaussy, and R. Rammal, J. Phys. (Paris) **44**, L853 (1983). B. Pannetier, J. Chaussy, R. Rammal, and J. Villegier, Phys. Rev. Lett. **53**, 1845 (1984). Early work on proximity-effect junction arrays appears, e.g., in C.J. Lobb, D.W. Abraham, M. Tinkham, and T.M. Klapwijk, Phys. Rev. B **26**, 5268 (1982); C.J. Lobb, D.W. Abraham, and M. Tinkham, *ibid.* **27**, 150 (1983); Ch. Leeman, Ph. Lerch, G.-A. Racine, and P. Martinoli, Phys. Rev. Lett. **56**, 1291 (1986); M.S. Rzochowski, S.P. Benz, M. Tinkham, and C.J. Lobb, Phys. Rev. B **42**, 2041 (1990); S.P. Benz, M.S. Rzochowski, M. Tinkham, and C.J. Lobb, Phys. Rev. Lett. **64**, 693 (1990). Work on tunnel-junctions appears, e.g., in M. Bushman, R.H. Cantor, J.M. Gordon, A.M. Goldman, and F. Yu, IEEE Trans. Magn. **MAG-23**, 1122 (1987); B.J. van Wees, H.S.J. van der Zant, and J.E. Mooij, Phys. Rev. B **35**, 7291 (1987); More recent results include A.L. Eichenberger, *et al.* Phys. Rev. Lett. **77**, 3905 (1996); S.E. Korshunov, R. Meyer, and P. Martinoli, Phys. Rev. B **51**, 5914 (1995); P. Martinoli *et al.*, Phys. Scr. **T49A**, 176 (1993); R. Theron *et al.*, Phys. Rev. Lett. **72**, 562 (1994); R. Theron *et al.*, *ibid.* **71**, 1246 (1993); R. Meyer *et al.*, *ibid.* **67**, 3022 (1991); Phys. Rev. B **40**, 11 374 (1989).

[2] A new form of extreme localization, without disorder and with nondispersive states, was derived by F. Nori and Q. Niu, in *Quasicrystals and Incommensurate Structures in Condensed Matter* edited by E. Gomez *et al.* (World Scientific, Singapore, 1990), p. 434, for decagonal Aharonov-Bohm cages. This type of localization is due to the effect of destructive quantum interference for tight-binding electrons subject to certain values of the applied magnetic field. This extreme form of localization without disorder has also been found in superconducting wire networks by J. Vidal, R. Mosseri, and B. Douçot, Phys. Rev. Lett. **81**, 5888 (1998); J. Vidal, P. Butaud, B. Douçot, and R. Mosseri, Phys. Rev. B **64**, 155306 (2001). The first experimental verification appeared in C.C. Abilio, P. Butaud, Th. Fournier, B. Pannetier, J. Vidal, S. Tedesco, and B. Dalzotto, Phys. Rev. Lett. **83**, 5102 (1999).

[3] F. Nori and Q. Niu, Phys. Rev. B **37**, 2364 (1988); P. Santhanam, C.C. Chi, and W.W. Molzen, *ibid.* **37**, 2360 (1988).

[4] J.M. Gordon, A.M. Goldman, J. Maps, D. Costello, R. Tiberio, and B. Whitehead, Phys. Rev. Lett. **56**, 2280 (1986); B. Doucot, Y.Y. Wang, J. Chaussy, B. Pannetier, R. Rammal, A. Vareille, and D. Henry, *ibid.* **57**, 1235 (1986); H.J. Lee, M.G. Forrester, M. Tinkham, and C.J. Lobb, Jpn. J. Appl. Phys., Part 1 **26**, Suppl. 26-3, 1385 (1987); J.M. Gordon and A.M. Goldman, Phys. Rev. B **35**, 4909 (1987).

[5] J.M. Gordon, A.M. Goldman, and B. Whitehead, Phys. Rev. Lett. **20**, 2311 (1987); R.G. Steinmann, B. Pannetier, Europhys. Lett. **5**, 559 (1988); J. Simonin and A. Lopez, Phys. Rev. Lett. **56**, 2649 (1986).

[6] E. Granato and J.M. Kosterlitz, Phys. Rev. B **33**, 6533 (1986); M.G. Forrester, H.J. Lee, M. Tinkham, and C.J. Lobb, *ibid.* **37**, 5966 (1988); S.P. Benz, M.G. Forrester, M. Tinkham, and C.J. Lobb, *ibid.* **41**, 8749 (1990).

[7] A. Behrooz, M. Burns, H. Deckman, D. Levine, B. Whitehead, and P.M. Chaikin, Phys. Rev. Lett. **57**, 368 (1986); Phys. Rev. B **35**, 8396 (1987); G. Grest, P.M. Chaikin, and D. Levine, Phys. Rev. Lett. **60**, 1162 (1988); M.A. Iztler, A.M. Behrooz, C.W. Wilks, R. Bojko, and P.M. Chaikin, Phys. Rev. B **42**, 8319 (1990).

[8] K. Springer and D. Van Harlingen, Phys. Rev. B **36**, 7273 (1987).

[9] F. Nori, Q. Niu, E. Fradkin, and S.J. Chang, Phys. Rev. B **36**, 8338 (1987).

[10] M.Y. Choi, J.S. Cheung, and D. Stroud, Phys. Rev. B **35**, 1669 (1987).

[11] N. de Bruijn, Proc. K. Ned. Akad. Wet., Ser. A: Math. Sci. **43**, 27 (1981); **43**, 53 (1981); For studies of the one-dimensional analog case see, for instance, F. Nori and J.P. Rodriquez, Phys. Rev. B **34**, 2207 (1986); Q. Niu and F. Nori, Phys. Rev. Lett. **57**, 2057 (1986); Phys. Rev. B **42**, 10329 (1990); M. Kolar, M.K. Ali, and F. Nori, *ibid.* **43**, 1034 (1991).

[12] See, e.g., P.G. de Gennes, C.R. Seances Acad. Sci., Ser. 2, **292**, 279 (1981); H.J. Fink, A. López, and R. Maynard, Phys. Rev. B **26**, 5237 (1982); J.M. Simonin, C. Wiecko, and A. López, *ibid.* **28**, 2497 (1983).

[13] W.Y. Shih and D. Stroud, Phys. Rev. B **28**, 6575 (1983); **30**, 6774 (1984); **32**, 158 (1985); D. Stroud and W.Y. Shih, Mater. Sci. Forum **4**, 177 (1985).

[14] Q. Niu and F. Nori, Phys. Rev. B **39**, 2134 (1989).

[15] Y.-L. Lin and F. Nori, Phys. Rev. B **50**, 15 953 (1994).

[16] V.V. Moshchalkov *et al.*, Nature (London) **373**, 319 (1995); C. Strunk *et al.*, Phys. Rev. B **53**, 11332 (1996); V. Bruyndoncx, C. Strunk, V.V. Moshchalkov, C. Van Haesendonck, and Y. Bruynseraede, Europhys. Lett. **36**, 449 (1996); C. Strunk *et al.*, Phys. Rev. B **54**, R12701 (1996); V.V. Moshchalkov, X.G. Qiu, and V. Bruyndoncx, *ibid.* **55**, 11793 (1997); C. Strunk *et al.*, *ibid.* **57**, 10854 (1998); V. Bruyndoncx *et al.*, *ibid.* **60**, 4285 (1999); V. Bruyndoncx, L. Van Look, M. Verschuere, and V.V. Moshchalkov, *ibid.* **60**, 10468 (1999); J.T. Devreese, V.M. Fomin, V.R. Misko, and V.V. Moshchalkov, Phys. Low-Dimens. Semicond. Struct. **1-2**, 33 (1998); V.M. Fomin, V.R. Misko, J.T. Devreese, and V.V. Moshchalkov, Physica B **249-251**, 476 (1998); Phys. Rev. B **58**, 11703 (1998).

[17] D.R. Hofstadter, Phys. Rev. B **12**, 2239 (1976).

[18] T. Geisel, R. Ketzmerick, and G. Petschel, Phys. Rev. Lett. **66**, 1651 (1991); **67**, 3635 (1991); G. Petschel and T. Geisel, *ibid.* **71**, 239 (1993).

[19] M.-C. Chang and Q. Niu, Phys. Rev. Lett. **75**, 1348 (1995); Phys. Rev. B **53**, 7010 (1996).

[20] Yi Xiao, D. A. Huse, P. M. Chaikin, M. J. Higgins, S. Bhattacharya, and D. Spencer, preceding paper, Phys. Rev. B **65**, 214503 (2002).

[21] M.J. Higgins, Y. Xiao, S. Bhattacharya, P.M. Chaikin, S. Sethuraman, R. Bojko, and D. Spencer, Phys. Rev. B **61**, R894 (2000).

[22] Kyungwha Park and David A. Huse, Phys. Rev. B **64**, 134522 (2001).

[23] P. Schiffer *et al.*, Phys. Rev. Lett. **74**, 2379 (1995); D. Davidovic *et al.*, *ibid.* **76**, 815 (1996); Phys. Rev. B **55**, 6518 (1997); I. Ritchey, P. Chandra, and P. Coleman, *ibid.* **47**, 15 342 (1993); P. Chandra, P. Coleman, and I. Ritchey, J. Phys. I **3**, 591 (1993).

[24] M. F. Laguna, C. A. Balseiro, D. Dominguez, and F. Nori, Phys. Rev. B **64**, 104505 (2001).

[25] F. Nori and Y.-L. Lin, Phys. Rev. B **49**, 4131 (1994); Y.-L. Lin and F. Nori, *ibid.* **53**, 13 374 (1996); Phys. Rev. Lett. **76**, 4580 (1996); Phys. Rev. B **53**, 15 543 (1996).

[26] For reviews of early work on this subject and extensive lists of references, see M.G. Blamire, J. Low Temp. Phys. **68**, 335 (1987); A.N. Lykov, Adv. Phys. **42**, 263 (1993).

[27] See, e.g., M. Baert *et al.*, Europhys. Lett. **29**, 157 (1995); M. Baert, *et al.*, Phys. Rev. Lett. **74**, 3269 (1995); E. Rosseel *et al.*, Phys. Rev. B **53**, R2983 (1996); J.I. Martin, M. Velez, J. Nogues, and Ivan K. Schuller, Phys. Rev. Lett. **79**, 1929 (1997); J.I. Martin, M. Velez, A. Hoffmann, I.K. Schuller, and J.L. Vicent, *ibid.* **83**, 1022 (1999); Y. Jaccard, J.I. Martin, M.C. Cyrille, M. Velez M, J.L. Vicent, and I.K. Schuller, Phys. Rev. B **58**, 8232 (1998); J.R. Martin, M. Velez, J. Nogues, A. Hoffmann, Y. Jaccard, and I.K. Schuller, J. Magn. Magn. Mater. **177**, 915 (1998).

[28] Commensurate transitions, producing peaks in $M(H)$, were found by J. Guimpel, L. Civale, F. de la Cruz, J.M. Murduck, and I.K. Schuller, Phys. Rev. B **38**, 2342 (1988). These early measurements, showing matching effects, were also explained by these authors calculating the Gibbs free energy with no adjustable parameters. Similar measurements were rediscovered later in high-T_c materials by C. Hünnekes *et al.*, Phys. Rev. Lett. **72**, 2271 (1994). See also S.H. Brongersma *et al.*, *ibid.* **71**, 2319 (1993).

[29] See, e.g., R. Fehrenbacher, V.B. Geshkenbein, and G. Blatter, Phys. Rev. B **45**, 5450 (1992); M.A. Itzler and M. Tinkham, *ibid.* **51**, 435 (1995).

[30] See, e.g., M. Oussena *et al.*, Phys. Rev. Lett. **72**, 3606 (1994).

[31] F. Nori, Science **278**, 1373 (1996); T. Matsuda, *ibid.* **278**, 1393 (1996); K. Harada *et al.*, *ibid.* **274**, 1167 (1996); C. Reichhardt *et al.*, Phys. Rev. B **54**, 16108 (1996); **56**, 14196 (1997); **58**, 6534 (1998); **57**, 7937 (1998); Phys. Rev. Lett. **78**, 2648 (1997); C. Reichhardt and F. Nori, *ibid.* **82**, 414 (1999).

[32] C. Reichhardt *et al.*, Phys. Rev. B **53**, R8898 (1996); **52**, 10441 (1995); C.J. Olson, C. Reichhardt, and F. Nori, *ibid.* **56**, 6175 (1997); Phys. Rev. Lett. **80**, 2197 (1998); **81**, 3757 (1998).

[33] D. Weiss *et al.*, Phys. Rev. Lett. **66**, 2790 (1991).

[34] See, e.g., E.A. Jackson, *Nonlinear Dynamics* (Cambridge University Press, Cambridge, England, 1991).

[35] A. Tonomura, Physica B **280**, 227 (2000); Int. J. Mod. Phys. B **15**, 3427 (2000); Mater. Charact. **42**, 201 (1999); Micron **30**, 479 (1999); Phys. Scr. **T76**, 16 (1998); A. Tonomura *et al.* Nature (London) **6717**, 308 (1999); **6847**, 620 (2001); Science **294**, 2136 (2001); C.H. Sow *et al.* Phys. Rev. Lett. **60**, 2693 (1998); N. Osakabe *et al.*, *ibid.* **78**, 1711 (1997).